AAPM REPORT NO. 200

The Design and Use of the ICRU/AAPM CT Radiation Dosimetry Phantom: An Implementation of AAPM Report 111

The Report of AAPM Task Group 200

January 2020

DISCLAIMER: This publication is based on sources and information believed to be reliable, but the AAPM, the authors, and the editors disclaim any warranty or liability based on or relating to the contents of this publication.

The AAPM does not endorse any products, manufacturers, or suppliers. Nothing in this publication should be interpreted as implying such endorsement.

© 2020 by American Association of Physicists in Medicine

This page intentionally left blank.

The Design and Use of the ICRU/AAPM CT Radiation Dosimetry Phantom: An Implementation of AAPM Report 111

The Report of AAPM Task Group 200

Donovan M. Bakalyar[1], Chair, Erin Angel[2], Kirsten Lee Boedeker[3], John Boone[4], Kish Chakrabarti[5], Huaiyu Heather Chen-Mayer[6], Dianna Cody[7], Robert Dixon[8], Sue Edyvean[9], Wenzheng Feng[10], Shuai Leng[11], Sarah McKenney[12], Michael McNitt-Gray[13], Richard Morin[14], J. Thomas (Tom) Payne[15], Robert Pizzutiello[16], Jeffrey Siewerdsen[17], Keith Strauss[18], and Paul Sunde[19]

Additional Contributors:

Lars Herrnsdorf, Marcus Söderberg, Rob Morrison, Elisabeth Nilsson, and George W. Burkett

[1]Henry Ford Health System, Detroit, MI
[2]Canon Medical Systems, Tustin, CA
[3]Canon Medical Systems, Los Angeles, CA
[4]University of California–Davis Medical Center, Sacramento, CA
[5]CDRH/FDA, Silver Spring, MD
[6]NIST, Gaithersburg, MD
[7]University of Texas MD Anderson Cancer Center, Houston, TX
[8]Wake Forest University, Winston-Salem, NC
[9]Centre for Radiation, Chemical and Environmental Hazards (CRCE), Chilton, Oxfordshire, UK
[10]Saint Barnabas Medical Center, Livingston, NJ
[11]Mayo Clinic, Rochester, MN
[12]Stanford University, Stanford, CA
[13]David Geffen School of Medicine at UCLA, Los Angeles, CA
[14]Mayo Clinic, Jacksonville, FL
[15]Midwest Radiation Consultants, Inc., Ora Valley, AZ
[16]Upstate Medical Physics (retired), Victor, NY
[17]Johns Hopkins University, Baltimore, MD
[18]Children's Hospital Medical Center, Cincinnati, OH
[19]Radcal Corporation, Monrovia, CA

DISCLAIMER: This publication is based on sources and information believed to be reliable, but the AAPM, the authors, and the publisher disclaim any warranty or liability based on or relating to the contents of this publication.

The AAPM does not endorse any products, manufacturers, or suppliers. Nothing in this publication should be interpreted as implying such endorsement.

ISBN: 978-1-936366-74-3
ISSN: 0271-7344

© 2020 by American Association of Physicists in Medicine

All rights reserved

Published by

American Association of Physicists in Medicine
1631 Prince Street
Alexandria, VA 22314

Contents

1. Background and Rationale 6
2. Glossary 6
3. Description of the ICRU/AAPM Phantom 7
3.1 Assembly of the Phantom 9
3.2 Alignment of the Phantom on the Table 9
4. Measurement Methodology 10
4.1 Background. 10
4.2 Determining D_{eq} and $H(L)$ 11
4.3 An Example Using Real-Time Data Acquisition 11
4.3.1 Using Real-Time Dose Measurements along the Axis 12
4.3.2 Using Real-Time Dose Measurements near the Periphery 12
4.3.3 Choosing Scanning Parameters for the Peripheral Dose Profile 14
4.3.4 Determining $h(L)$ for Small Values of L 15
5. Step-by-Step Procedure for Measurements on the Phantom 15
5.1 Data Acquisition, Single Scan Method 15
5.2 Data Acquisition, Serial Method 16
5.3 Additional Collimations and Pitch Values 16
5.4 Data Analysis 16
5.5 Comparison to $CTDI_{100}$ Measurements 17
6. Practical Implementation of the Measurement Methodology 18
6.1 Measurements in the Full (3 Sections, 60 cm Length) Phantom. 18
6.2 Measurements in a Single Section of the ICRU/AAPM Phantom 18
6.3 Measurements in Air 18
6.4 Measurements in Very Wide Beams and Using Stationary Tables 20
7. Conclusions 21
8. References 21
Appendix 1: Measurements in Other Geometries 23
Appendix 2: Measurement Equipment Note 24
Appendix 3: Supplemental Material Available 25
Data Recording 25
Animations 25
Tutorial and Example for Fine-Tuning the Determination of D_{eq} 25
Machine Drawings for Phantom 25
Appendix 4: Corresponding Human Size using Water-Equivalent Diameter 33
Appendix 5: Fine Tuning D_{eq} 35

1. Background and Rationale

Although the CTDI phantom and its associated pencil ionization chamber measurement methodology have proven to be very useful, they suffer from limitations that have been critically examined over the past several years. As a consequence, Task Group 111 was formed by the AAPM to address some of the concerns that had been raised. Among these concerns are the following:

1. $CTDI_{100}$ is a surrogate for the dose at the center of a scan of a single, fixed length, 100 mm, and excludes the dose that would accumulate for longer scans. "This underestimation is systematic, applying to narrow and wide beams alike, and slowly becomes larger with increasing width of the z-axis collimation."[1]
2. Some scanners employ very wide beams, approaching or even wider than the length of the 100 mm pencil chamber, rendering the CTDI paradigm completely unsuitable for characterizing the dose.
3. CTDI may be inappropriate for stationary table applications, particularly for beams wider than 100 mm. AAPM Report 111[1] offered several recommendations for a new measurement methodology and suggested several phantom designs.

Task Group 200 and the ICRU's Committee on Radiation Dose and Image-Quality Assessment in Computed Tomography have jointly developed a phantom design and robust measurement schemes that follow the methodology of AAPM Report 111 and are suitable for a wide range of CT scanner designs and scanning conditions. Several prototype phantoms were built by a research group at the University of California–Davis (UC Davis), and these phantoms have been tested at several centers around the United States as well as in England.

The purpose of this current report is to (a) describe the design of the phantom and (b) suggest a broadly applicable measurement methodology that overcomes the limitations of $CTDI_{100}$ and the metrics derived from it, such as $CTDI_{vol}$. The resulting measurement procedures have been developed for conventional MDCT scanners, including models with wide (16 cm, for example) beams. However, the application of this methodology to flat panel and specialized cone-beam CT systems presents special challenges that are briefly discussed in Appendix 1. The solutions to these particular problems are beyond the scope of this report.

2. Glossary

Table 1: Definitions and notations used in this report

a	Width along the axis of rotation of the pre-patient z-axis collimator geometrically projected from the centroid of the x-ray source. Parameter a is the full width of the beam at half its value at $z = 0$.
a_w	The widest beam width available for a particular scanner.
α	Dimensionless fit parameter associated with the magnitude of the exponential term in $h(L)$. $1-\alpha$ is the magnitude of the approach-to-equilibrium function $H(L)$ at $L = 0$. See Equations 9–11.
b	In axial scanning, b is the midpoint-to-midpoint spacing between successive scans. In helical scanning, b is the table travel per rotation.
D_{eq}	The equilibrium, or limiting dose at a point in an infinite phantom for an infinite scan. (It will be dependent on the radial distance of that point.) For the ICRU/AAPM phantom it is the absorbed dose at a point in the mid plane for a scan centered there and of sufficient length to not change significantly with further increases in scan length. It is fully described in AAPM Report 111.
$D_{eq,c}$ and $D_{eq,e}$	D_{eq} determined at the central and periphery (edge) of the phantom, respectively.
$\overline{D_{eq}}$	The spatial average of D_{eq} as expressed in Equation 2.

Table 1: Definitions and notations used in this report

$D_L(0)$	Cumulative dose at longitudinal position $z = 0$, viz., at the midpoint (central plane) of a scanning range of length L. It is fully described in AAPM Report 111.
D^*	D^* is an estimate of D_{eq} used in an iteration procedure. It ultimately converges to D_{eq}.
$g(L,D^*)$	Is defined as $\log_2[1 - h(L)/D^*]$. This is a straight line if $D^* = D_{eq}$ for values of L significantly larger than the beam width a.
$h(L)$	$D_L(0)$. This representation of $D_L(0)$ is used in ICRU Report 87 in order to present the behavior of the dose integral as a function of scanning length in a more conventional mathematical form.
$h_c(L)$ and $h_e(L)$	The function $h(L)$ determined at the central and peripheral (edge) positions of the chamber within the center section of the phantom, respectively.
$H(L)$	$h(L)/D_{eq}$. Approach-to-equilibrium function. In AAPM Report 111, the lowercase h is used. We are following the convention introduced by ICRU Report 87.
$H_c(L)$ and $H_e(L)$	The function $H(L)$ determined at the central and peripheral (edge) positions of the chamber within the center section of the phantom, respectively.
K	Air kerma measured by dosimeter; typically expressed in mGy.
κ	Area-averaged CT number for the cross section of interest. (CT number is universally measured in the dimensionless Hounsfield Units.)
ℓ	The length of the ion chamber or other dosimeter used for phantom measurements. The length is measured in the z direction, i.e., parallel to the axis of rotation.
L	The length of the irradiated region. It is centered about the mid-plane of the phantom or about the irradiated region in an infinite phantom.
$L_{½}$	The half-length of L. This is the value of L for which the exponential in Equation 9 is equal to ½.
L_{eq}	The finite scanning length in AAPM Report 111 for which the cumulative dose is deemed to be close enough to D_{eq} for practical purposes. From Equation 9, $L_{eq} = [4/\ln(2)] \times L_{½} = 5.77 \times L_{½}$.
mAs_{eff}	Effective mAs (effective tube current-time product). This is the product of the tube current and the rotation time divided by the pitch.
nT	Sometimes referred to as the *collimation*. nT is that portion of the beam width, measured along the axis of rotation, which is intercepted by the active detectors and used to create images. nT is always less than the full beam width a in that there is always some *overbeaming* to guarantee that the active part of the detector is completely within the beam. (nT can be broken up into n data acquisition rows, each of projected width T.)
p	Pitch. Here the definition is generalized to apply to either axial or helical scanning. The pitch is the ratio $b/(nT)$.
r	Radial distance from the axis of the phantom.
r_e	Radial distance for the measurement near the edge (periphery) of the phantom. r_e = 13.37 cm for the ICRU/TG200 phantom.
z	The coordinate axis coincident with the axis of rotation of the gantry. $z = 0$ locates the central plane, i.e., the midpoint in a range of scanning over length L. For scanning without table translation, $z = 0$ locates central plane of the scanner. (For this report, scans using a tilted gantry will not be considered. That is, the direction of table travel will always be parallel to the axis of rotation.)

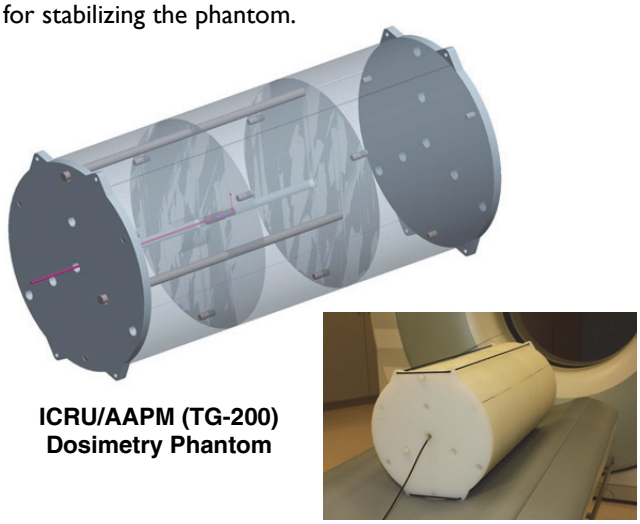
3. Description of the ICRU/AAPM Phantom

The assembled ICRU/AAPM phantom is shown in Figure 1. It can be divided into three sections to make it more manageable. When assembled, the three sections form a cylinder 30 cm in diameter and 60 cm in length. The phantom is made of high-density (0.97 g/cm^3) polyethylene, which was selected because it is (a) relatively light in weight, (b) closely mimics the absorption properties of human adipose tissue, and (c) is readily available and relatively inexpensive. In addition, at the particular diameter of 30 cm, Monte Carlo calculations show that the dose *in-medium* (as opposed to the air kerma) at the phantom's center is nearly the same as it would be for a water phantom of the same diameter.[1]

Each of the three sections has a mass of around 13.7 kg (weighing about the same as a fully assembled 32-cm CTDI phantom). Thus, when assembled, the total mass is 41.1 kg (around 91 lb). Channels, parallel to the cylinder axis, are bored deep into the phantom so that a radiation dosimeter can be positioned within the central transverse plane of the phantom, as shown in Figure 1.

Figure 2 shows the three sections of the phantom separated. Section A has channels running the length of its section to allow a dosimeter and cable to be inserted through its full length. Section B also has channels running its entire length so that a dosimeter can be inserted to a location corresponding to the center of the assembled phantom's full length; a plug less than half the length of the section is used to ensure that the center of the dosimeter is centered within the phantom. Section C is solid and is used primarily as a scatter medium in the context of dose measurements. There are three small holes located near the outer edge of the section faces. Locating pins are inserted into these holes whenever two sections are joined together. Rods are provided to fill the channels when they do not contain a radiation dosimeter. Detailed machine drawings of the entire phantom are provided as a part of Appendix 3.

Figure 1. The upper drawing shows a semi-transparent view of the phantom with its three sections along with the three channels for a radiation dosimeter. The lower drawing is a photograph of an assembled phantom. Note the dosimeter cable exiting the central channel. In addition to the three sections are end caps with support cording for holding the assembly together; these caps also have feet for stabilizing the phantom.



Convention: For this report, the term *dose* is not the absorbed dose to the phantom material, but rather the absorbed dose to the air in the ion chamber[1,2], as is the custom for $CTDI_{vol}$. In the diagnostic x-ray range, this is essentially equal to the *air kerma*[3]. Both the terms *absorbed dose* and *air kerma* will be used in this report. For dosimeters that are not ion chambers (e.g., solid state), equivalence to ion chambers will be provided by the manufacturer.

Because of the modular nature of the described phantom, it is possible to create a phantom configuration consisting of three sections of Section A. This creates channels running the entire 60-cm length of the phantom and facilitates axial dosimeter translation along the length of the phantom, as described in Appendix 1. More detailed information is available in ICRU Report 87[4].

Figure 2. Three sections of the phantom are displayed. They differ somewhat in design to allow for multiple uses. Sections A and B have channels to allow centering the dosimeter within the phantom. Section B also contains a blind hole for alternate materials or test objects. Section C is left blank to facilitate noise measurements. Three holes near the edge of the face of each section are provided so that small locating pins can be used to join the sections together.



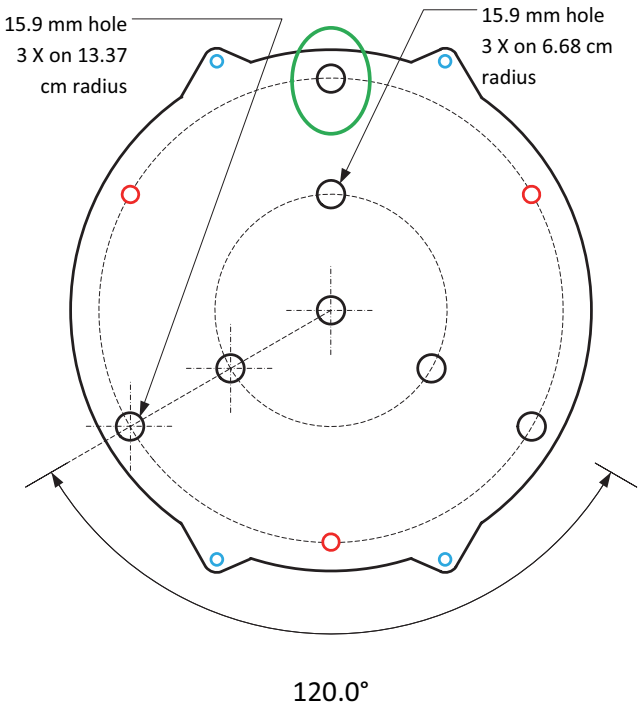


Figure 3. End cap plate. These are located on each end of the assembled phantom. There are three 15.9-mm (5/8") holes located around the periphery at a radius of 13.37 cm. If the table is flat, the hole (circled in green) located between a pair of feet can be aligned with the long dosimeter channel. Then the opposite pair of feet resting on the flat surface provides stability for measurements in the 12 o'clock position. For conventional concave tables, however, this choice will cause the phantom to sag in the middle. In this case, the solution is to align another of the three holes with the channel so that the feet are not in contact with the table. Then towels can be used to stabilize the phantom. (This figure was taken from University of California at Davis machine drawings.)

3.1 Assembly of the Phantom

The three sections are lifted to the CT table separately for assembly. Rotate sections A and B along their longitudinal axis to align the channels. Three small locating pins are positioned in matching holes around the periphery to join the two sections together. The sections are pressed together to completely close the gap between them. The process is repeated for the junction between sections B and C; in this case, there are no channels to match.

End caps, constructed from 12.7-mm-thick polyethylene plates, are positioned at the ends of the phantom with locating pins (described earlier) using the holes indicated in red in Figure 3. There are seven 15.9-mm (5/8") holes, depicted in black in Figure 3, which can be lined up with the three dosimeter channels with the peripheral channel in the 12 o'clock position. There are three possible orientations. The configuration depicted in Figure 3 has the peripheral hole (circled in green) aligned with the outer channel and centered between two foot protrusions. This offers stability on flat tables, but for conventional concave tables, the phantom will sag in the middle. Here one of the other orientations should be used so that the feet are not in contact with the table. Towels may be used for stability. The small holes in the feet, depicted in blue, may be used for threading the provided bungee cord, which helps hold the assembly together (see Figure 1). Once assembled, the phantom should be examined carefully to be sure there are no gaps between the sections. Three of the 15.9-mm holes are at a radius of 6.68 cm and are for access to the channel in the intermediate position. An identical 15.9-mm hole is used for the center dosimetry measurements.

3.2 Alignment of the Phantom on the Table

The axis of the phantom should be aligned to coincide with the gantry axis of rotation, the z-axis. The peripheral dosimeter channel should be in the 12 o'clock position, as indicated by the green circle in Figure 3. Making edge measurements at the 12 o'clock position minimizes the effect of the table. (This is the same consideration that is made for CTDI measurements.) The phantom is long, and so its

alignment with system isocenter should be assured by moving the table back and forth within the gantry, checking the alignment of the phantom from end to end.

4. Measurement Methodology

4.1 Background

As discussed in detail in AAPM Report 111[1], a procedure of central importance consists of positioning a small dosimeter in the central plane of the full (60 cm) phantom and performing a helical scan along the entire length of the phantom [RUN MOVIE # 1]. A series of shorter scans, with each going from $-L/2$ to $+L/2$ in the z direction, can also be performed, resulting in a sampling of the cumulative absorbed dose as a function of its scan length[1,4]. This function, $h(L)$, is displayed in Figures 4, 5b, 6, and 7b. It shows that at $L = 600$ mm, the absorbed dose is asymptotically approaching the *equilibrium dose* D_{eq}, the value of $h(L)$ for an infinite scan. A close inspection of these curves, however, shows that $h(L)$ hasn't quite flattened out, and that for each case, especially those in Figures 4 and 5b, a small increase would be expected for longer scans. Fortunately, the predictable behavior of the function makes it possible to estimate this residual absorbed dose using the graphical technique presented in Appendix 5. There it also shows that for the test results illustrated in Figures 4, 5b, and 7b, $h(L = 600$ mm) is within 1.5% of D_{eq}. Normalizing $h(L)$ to D_{eq} gives rise to the *approach-to-equilibrium* function, $H(L) = h(L)/D_{eq}$. (We are following the ICRU Report 87 convention[4] for representation of $h(L)$, which differs somewhat from that used in AAPM Report 111.) This series of scans of varying length L is the **Serial Method** for obtaining D_{eq}, $h(L)$, and $H(L)$, with each scan yielding a single point on the $h(L)$ curve.

A much better method, the **Single Scan Method**, is to perform only one scan through the full length of the phantom while recording the instantaneous *air kerma rate, dK/dt,* using a real-time dosimeter. Dividing dK/dt by the known (constant) table speed, dz/dt, gives us the air kerma per distance dK/dz at each position z, with $z = 0$ set to the center of the dosimeter positioned in the central plane of the phantom. (This should correspond closely to the peak value of dK/dz.) This function, displayed in Figures 5a and 7a, can be integrated from $-L/2$ to $+L/2$ for any L up to the length of the phantom; this process yields $h(L)$, shown in Figures 5b and 7b, all the way up to $L = 600$ mm.

Note that table speed (distance/time) is often given directly on the scanner or *may* be given in the DICOM metadata at (0018,9309). (Caution! The term "table speed" is often used to indicate the distance per rotation.) From the definition of pitch, table speed is (pitch × nT) / (rotation time). (Any

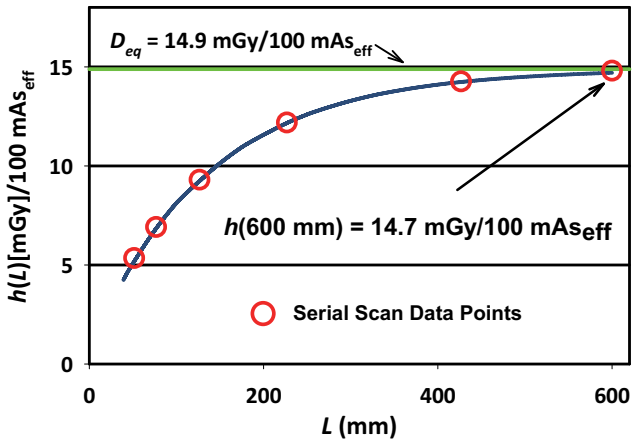


Figure 4. Cumulative air kerma as a function of increasing scan length. The serial method was used to acquire the six points in red; the blue curve was obtained from single scan data. As the scan length increased, D_{eq}, indicated by the horizontal green line, is approached. (The data was taken on a Siemens AS+ at a tube potential of 120 kV. The collimation (nT) was 38.4 mm. The measured $CTDI_{vol}$ was 7.1 mGy/100 mAs_{eff}.)

doubts over which parameter is actually being displayed by the machine may be resolved by measuring the table speed directly using a tape measure and a stopwatch.)

4.2 Determining D_{eq} and $h(L)$

Both the serial and single scan methods use a small dosimeter embedded in the central plane of the phantom. (The measurements presented in this document were obtained using a small thimble ion chamber, 0.6 cc in volume and 19.7 mm in length (Radcal 10X5-0.6CT). Other dosimeters are described in Appendix 2.) For the serial method, integrating electronics provide the accumulated air kerma for each scan. This approach was used to acquire the six points in red on the $h(L)$ curve in Figure 4. The single scan method requires electronics that can deliver the instantaneous air kerma rate. The single scan method was used to determine the blue curve in Figure 4. The limiting value D_{eq} is approached as L grows in length with $h(600\text{ mm}) = 14.7$ mGy/100 mAs_{eff}. This is well within 1.5% of 14.9 mGy/100 mAs_{eff}, the value for D_{eq} determined using the method of Appendix 5.

The equivalence of the two techniques is confirmed by the data shown in Figure 4. While the serial method is directly analogous to patient scanning, it is overly burdensome; a separate scan is required for every point on the $h(L)$ curve. On the other hand, the single scan method yields the entire curve with one pass and should, therefore, be used whenever possible.

Though L for the single scan method is simply the distance between the limits of integration, L for the serial method can be affected by complications, such as overscanning and active collimation. Since these considerations also apply to patient scanning, the definition of L must be general enough to include both techniques, even though $h(L)$ is to be determined using the single scan method whenever possible. Thus it is valuable to think in terms of generalizing the concept of *directly irradiated length*. This term was introduced by Dixon and Boone[5] to underscore the equivalence between two common scanning methods: (1) a conventional scan using a moving table to irradiate a length longer than a, the width of the beam at the axis of rotation, and (2) a fixed table where the irradiated length *is* the beam width a. Application of this concept can be broadened further since only the length that was directly irradiated is important, not the details as to how this was accomplished. (When the scan is complete, the important question to ask is, "What was the *irradiated length*?")

For helical scans, the International Electrotechnical Commission (IEC) Glossary[6] defines the dose-length product, DLP, as $\text{CTDI}_{\text{vol}} \times L$. In this glossary, L (taken from IEC 60601-2-44, Ed. 3) is described as "the FWHM along a line perpendicular to the tomographic plane at isocenter of the free-in-air dose profile for the entire scan." This description is consistent with the concept of irradiated length, as described in the previous paragraph. Since values for CTDI_{vol} and DLP are provided by the CT scanner, $L = \text{DLP}/\text{CTDI}_{\text{vol}}$ is the value to be used for helical scans. This is how L was determined for Figure 4, and there was excellent agreement between the two methods for several other manufacturers and models using this definition as well[7]. (Note: the *Exposed Range*, defined in Part 16 of the DICOM Standard[8] for use in CT radiation dose structured reports, is taken from the same IEC report and so should be equal to the calculated value of L above. Again, this definition is for helical scans only, and so it is a special case of the general concept of irradiated length.)

4.3 An Example Using Real-Time Data Acquisition

The following describes the measurement of $h(L)$ using the single scan method (a) at the central axis and (b) at the edge position, which is near the periphery at the point (12 o'clock) farthest from the table.

Figures 5 and 7 show the data taken from helical scans of the AAPM/ICRU phantom on a Philips Brilliance 6 CT machine. The data was acquired using Radcal Accu-Gold electronics with a 10X5-0.6CT ion chamber. Scans were performed at a tube potential of 120 kV, a tube current of 105 mA, a rotation time of 0.5 s, a pitch of 0.656, and a collimation, nT, of 4.5 mm (6 × 0.75 mm detector config-

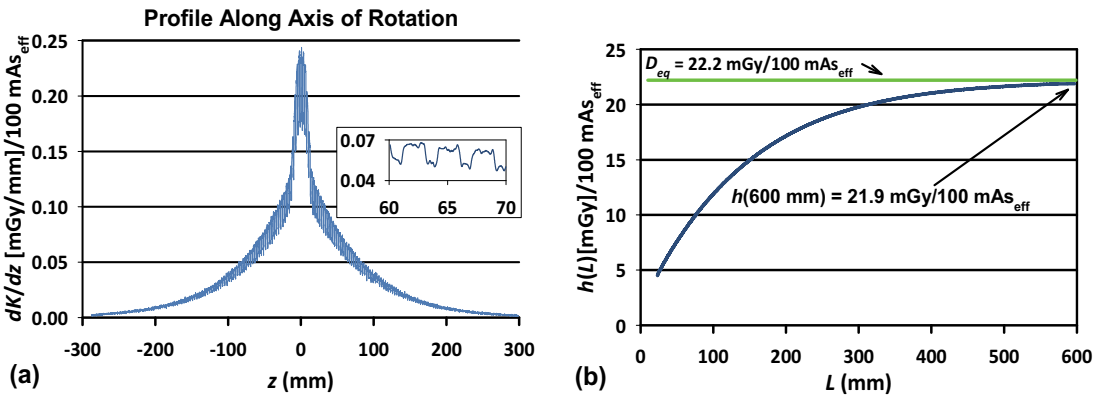


Figure 5. (a) Air Kerma rate profile recorded using a Radcal Accu-Gold digitizer and 10X5-0.6CT ion chamber on a Philips Brilliance 6 CT scanner. Inset shows the effect of the table during rotation. (b) Integral of the profile as a function of scan length where the scan length is centered on the peak position (0 mm in the top graph) of the profile. As the scan length increases, the limiting value D_{eq} is approached. The measured $CTDI_{vol}$ was 10 mGy/100 mAs_{eff}.)

uration). The effective tube current-time product, mAs_{eff}, = 0.5 s × 105 mA/0.656 was 80. The table travel per rotation b was pitch × collimation = 4.5 mm × 0.656 = 2.95 mm/rotation. The table speed, 5.904 mm/s, is b divided by the rotation time. (The scanner reported $CTDI_{vol}$ for these scans, confirmed by measurement, was 10 mGy/100 mAs_{eff}. Note that for the central axis scan for the Philips scanner in Figure 5, the ratio $D_{eq}/CTDI_{vol}$ is close to that for the Siemens scanner in Figure 4.)

4.3.1 Using Real-Time Dose Measurements along the Axis

Figure 5a shows dK/dz as a function of position z, obtained along the central axis of the AAPM/ICRU phantom. (The table speed has been used to convert dK/dt and time, as described in section 3.1.) Figure 5b is a plot of the integral taken over $\pm L/2$ about the center of the peak of the profile shown in Figure 5a. A limiting value is approached as L is increased beyond 500 mm. (Applying the standard CTDI methodology on this phantom where the table is stationary, the 100-mm pencil chamber would capture only a single point, h(100 mm), on the $h(L)$ curve of Figure 5b. This point is the integral of the dK/dz data between –50 mm and +50 mm in Figure 5a.)

Although at first glance the profile in Figure 5a appears to be noisy, most of the amplitude fluctuations are due to the table attenuation occurring during part of every gantry rotation. The contribution to dK/dz due to table attenuation is modulated at a spatial frequency of $1/b$. This effect is shown in the inset where a magnified 10-mm portion of the profile is shown. The table travel per rotation b was short enough so that the cyclic variation due to table modulation is almost completely smoothed over by the integration process, giving rise to the smooth curve in Figure 5b.

As L increases, the dose approaches its equilibrium value D_{eq}, as is shown in Figure 5b. Normalizing this whole curve to D_{eq} transforms it into the "approach to equilibrium" curve $H(L)$. It is interesting to note that the $H(L)$ plots along the central axes for the Siemens and Philips scanners of Figures 4 and 5 are close to identical, as is shown in Figure 6. Whether this very close agreement is a coincidence or occurs over a range of models and detector positions is beyond the scope of this report. (Related measurements have shown $H(L)$ to be quite insensitive to variations in tube potential[4].)

4.3.2 Using Real-Time Dose Measurements near the Periphery

For the edge scan, the dosimeter is positioned near the periphery in the 12 o'clock position, as indicated in Figure 3, and a scan through the entire cylinder is performed as before [RUN MOVIE # 2].

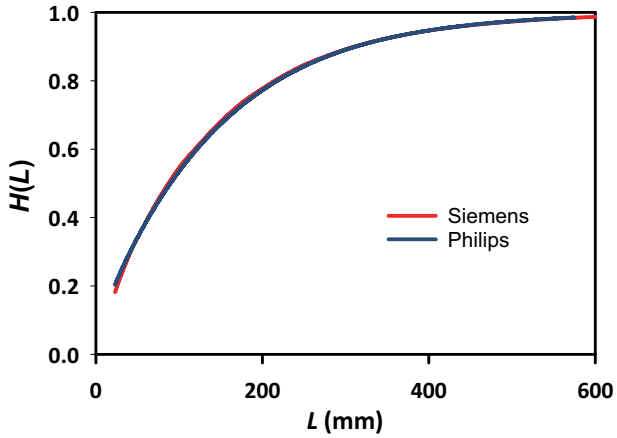


Figure 6. The normalized approach-to-equilibrium function for the Siemens scanner of Figure 4 and the Philips scanner of Figure 5. Note that the two curves are virtually identical.

As illustrated in Figure 7a, the envelope of dK/dz has the same general shape as that of the center, but there is a much more pronounced modulation with a periodicity of the table travel per rotation b. This modulation has several causes:

1. From the point of view of the moving x-ray source positioned on the rotating gantry, the dosimeter moves in and out of the shadow of the phantom. This has the largest effect.
2. As the x-ray source rotates, the source-dosimeter distance also varies, resulting in an inverse-square law variation. With the dosimeter in the 12 o'clock position, this effect enhances #1 since the dosimeter is farthest from the source when the phantom is largely between the source and dosimeter.
3. The table adds attenuation to that of the phantom during part of the rotation, so it has much in common with #1. (Table attenuation is the *only* listed modulation effect that also occurs for helical measurements along the central axis.) With the dosimeter at the 12 o'clock position, the additional table attenuation occurs when the beam intensity at the dosimeter is already greatly reduced by effects 1 and 2; thus, the additional reduction in overall dose due to table attenuation is small.
4. Near the surface of the cylinder, the dose may vary in the z direction due to inhomogeneity in the beam itself or from a mismatch between b and the beam width at the dosimeter radius. (A high pitch would lead to gaps and a low pitch would lead to overlap during successive rotations.) This can result either in irradiation gaps or beam overlap, as discussed in detail by Dixon[9].

The $h(L)$ curve obtained from the peripheral dK/dz data of Figure 7a is shown in Figure 7b. We notice that $h(L)$ approaches D_{eq} earlier than for the central scan of Figure 5. More precisely, it is half way to its limiting value in 30 mm, whereas for the central axis $h(L)$ curve, L must be all the way out to 87 mm before the dose is half of D_{eq}. As explained in the more detailed analysis in Appendix 5, this is because $H(L)$ starts out (near $L = 0$) at a substantially higher value at the edge than it does at the center. (A visual comparison of Figures 5a and 7a confirms that a much larger fraction of the integral occurs within the central portion of the scan for Figure 7a.) Appendix 5 also shows, however, that the half-length, $L_{½}$, characterizing the exponential part of the curve, is virtually the same at all radii.

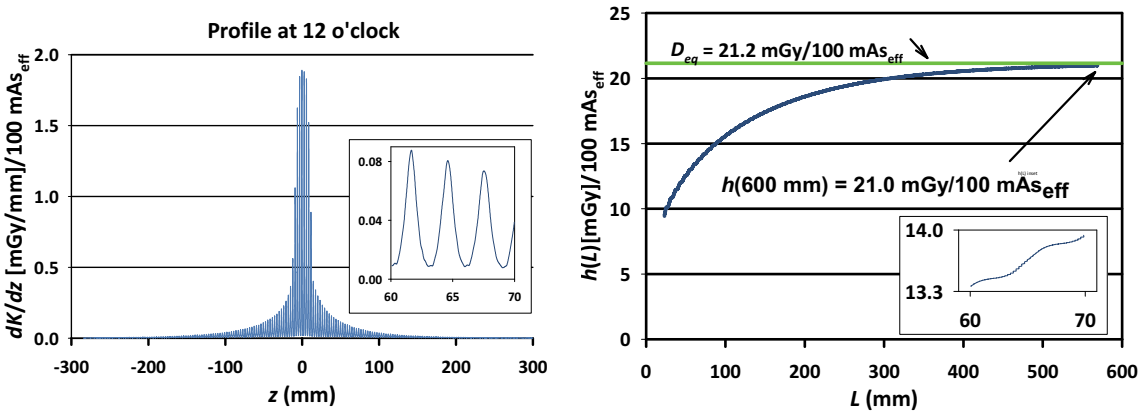


Figure 7. Similar to Figure 5, but with the sensor near the top edge of the cylinder (12 o'clock position) rather than at the center. (a) From the point of view of the x-ray source on the rotating gantry, the sensor moves in and out of the shadow of the phantom with the modulation approaching 100% as is shown in the inset. (b) The integral is similar to that in Figure 5b, but the direct radiation portion of the dose is much more dominant. Because of the high modulation frequency, the curve is quite smooth, despite the high modulation amplitude. (The tiny steps, barely distinguishable at the beginning of the $h(L)$ curve, are due to this modulation. The inset shows these wavy steps under high magnification.)

4.3.3 Choosing Scanning Parameters for the Peripheral Dose Profile

Figure 7a shows the profile for a helical scan measured with the dosimeter positioned at r_e, the radius (13.37 cm) near the edge (periphery) of the phantom. Ideally the average air kerma rate for the entire circle at r_e would be measured for each instant[1,9] as the phantom is scanned, but the chamber is only sampling one point on the circle at a time and requires integrating over a complete rotation to determine the average. Thus it is important to keep b, the table travel per rotation, small in order to properly sample the air kerma rate profile. For Figure 7, the beam collimation, nT, was 4 mm and the pitch, p, was 0.656, resulting in a value for b (= pnT) of 2.6 mm. Despite the high-modulation amplitude, the short distance per gantry rotation allows integration to very effectively smooth out the modulation on the $h(L)$ curve in Figure 7b. On this curve, the residual effect of these large excursions results in steps that are barely noticeable on the $h(L)$ curve. (The magnified view in the inset to Figure 7b displays these steps more clearly.)

Contrast these tiny steps with the prominent steps displayed in Figure 8b. Here, the table movement per rotation due to the collimation, nT, of 32 mm and the pitch, p, of 0.828 is pnT = 26.5 mm. This larger value of b results in the sparse sampling of the dose rate profile demonstrated in Figure 8a.

As discussed in AAPM Report 111, it is desirable that $p \le \ell/(2nT)$, where ℓ is the length of the dosimeter (in the z direction), in order to smooth out spatial variations at the surface for the peripheral acquisition. For Figures 5 and 7, where ℓ = 19.7 mm, this criterion was easily met. A true point chamber would not, of course, integrate out these spatial variations. Some solid state dosimeters that are candidates for these measurements are so small that the pitch criterion cannot be met. A variety of approaches are being considered for dealing with this difficulty (see Appendix 2).

It is interesting to note that the D_{eq} values determined here were within half a percent of values obtained scanning through the length of the phantom using a standard 100-mm CT pencil chamber [RUN MOVIE # 3] for the dosimeter. The longer chamber, though not suitable for acquiring the dose rate profile, is very effective for integrating out spatial variations since it satisfies the $p \le \ell/(2nT)$ crite-

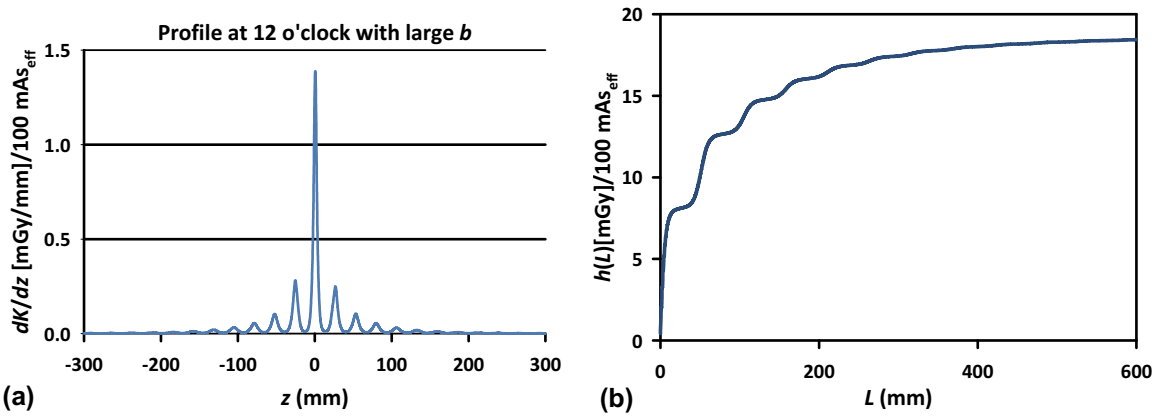


Figure 8. This figure demonstrates the consequence of using a table movement per rotation b that samples the dK/dz envelope too sparsely. Here b = 26.5 mm, and upon integrating to determine $h(L)$, prominent wavy step artifacts are introduced. (This data is from a Toshiba Aquilion One and acquired before the benefit of a high spatial sampling frequency 1/b was fully appreciated.) Contrast these steps with the almost unnoticeable steps in the $h(L)$ steps of Figure 7b.

rion to an extreme extent. It does require, however, that the phantom is long enough to closely approach equilibrium over the active length of the chamber.

4.3.4 Determining h(L) for Small Values of L

The early part of the curve was left out of the $h(L)$ plots in Figures 5b and 7b since, for very short values of L, the beam width and finite dosimeter length are not properly accounted for with a direct integral of the profile in determining the peak dose. In this case the most important limitation is the length of the ion chamber, ℓ = 19.7 mm, and so the curves were not shown for L values less than that. However, it should be noted that the functional behavior of $h(L)$ as L approaches zero applies to the very important case with no table motion and small beam widths (e.g., interventional procedures). Here the irradiated length is the beam width a, and $h(a)$ is the air kerma in the center of this beam (at $z = 0$).

Proper deconvolution may allow for the use of the $h(L)$ curves for very short irradiation lengths, including all of those typically used in interventional scanning with the table top in a fixed position. Alternatively, $h(a)$ could, for small a, be determined directly by using a stationary table and measuring the air kerma at $z = 0$. Here, though, the dosimeter length ℓ needs to be significantly smaller than a.

5. Step-by-Step Procedure for Measurements on the Phantom

5.1 Data Acquisition, Single Scan Method

1. Assemble the phantom and align it at isocenter in the coronal and sagittal planes in accordance with the instructions given in sections 2.1 and 2.2.
2. Select a collimation (nT), tube potential, rotation time, tube current, and pitch, keeping in mind the guidance given above for the requirements for the peripheral scan. (In the interest of simplicity, the scan along the central axis should have the same parameters as for the peripheral scan.)
3. Position the small radiation dosimeter in the center of the center section of the phantom and perform a helical scan through the entire phantom using a real-time dosimeter/electrometer

combination. The real-time data and table speed can be used to determine dK/dz, as described earlier.

4. Repeat for all tube potentials and bowtie/flat filter combinations of interest.

5. Position the small dosimeter in the central plane of the phantom at radius r_e in the 12 o'clock position. Perform a helical scan through the entire phantom using a real-time dosimeter/electrometer combination. Again, the real-time data and table speed can be used to determine dK/dz, as described earlier.

6. Repeat for the tube potentials and bowtie/flat filter combinations used in step 4.

5.2 Data Acquisition, Serial Method

With the setup the same as above, the serial scan method could be used as an alternative. The integrated dose for each scan as a function of increasing scan length is the function $h(L)$ where L = DLP/$CTDI_{vol}$, as described in section 3.1. As previously stated, the single scan method should be used wherever possible.

5.3 Additional Collimations and Pitch Values

As discussed in detail in AAPM Report 111 and the references cited therein, (particularly Dixon, Munley and Bayram[10] and Dixon and Ballard[19]) the results for all collimations and all pitch values are readily determined from the particular values chosen for the measurements at one specific collimation and pitch. Note that these results are robust, even in the presence of the heel effect. Thus, the collimation and pitch utilized for measurement should be chosen to meet the requirements discussed above (i.e., a small value for b) to ensure accuracy.

5.4 Data Analysis

1. For the long helical scans, dK/dz can be determined from the recording of dK/dt and the table speed, as described above.

2. If the real-time chamber is used, the integrated value may also be displayed directly for a useful check of the numerical integration. This should be recorded along with the dose rate data.

3. The zero of the distance scale is set to mid-peak of the dose profile, which occurs when the dosimeter is passing through the center of the beam. A further refinement is to view the dose profile data using a log scale for the ordinate and using that to determine the approximate center of symmetry.

4. The dose rate profile $dK/dz(z)$ is integrated from $-L/2$ to $+L/2$. The result is plotted as a function of L, where L is varied from zero to a value such that the integral no longer increases with integration length. The resultant function is $h(L)$, and its limiting value is, of course, D_{eq}. When $h(L)$ is divided by D_{eq}, the approach to equilibrium function $H(L)$, which varies from zero to 1, is obtained.

5. For the serial method described in 4.2, specific points of the $h(L)$ curve are obtained directly. To get $H(L)$, divide by D_{eq}, the value for a scan encompassing the entire phantom.

Both the central and edge functions $h_c(L)$ and $h_e(L)$, respectively, are to be retained. Equivalently, we can retain $H_c(L)$ and $H_e(L)$ along with their limiting values, $D_{eq,c}$ and $D_{eq,e}$, respectively. The $H(L)$

values alone are not enough since the central and edge values have different limits. For example, if we estimate the spatial average value of $H(L)$ with the familiar 1/3 and 2/3 coefficients from $CTDI_{vol}$,

$$\bar{h}(L) = \tfrac{1}{3} h_c(L) + \tfrac{2}{3} h_e(L) . \quad (1)$$

The important parameter $\overline{D_{eq}}$ from AAPM Report 111 can be expressed as

$$\overline{D_{eq}} = \lim_{L\to\infty} \bar{h}(L) = \tfrac{1}{3} D_{eq,c} + \tfrac{2}{3} D_{eq,e} . \quad (2)$$

Then

$$\overline{H}(L) = \frac{\bar{h}(L)}{\overline{D_{eq}}} , \quad (3)$$

where $\overline{H}(L)$ is an estimate of the spatial average of H over the entire cross section at position L.

5.5 Comparison to $CTDI_{100}$ Measurements

Table 2 lists the center-to-edge ratios for conventional $CTDI_{100}$ measurements (made using a 100-mm pencil chamber and a stationary table) on standard CTDI phantoms. For comparison, the L = 100 mm values from the data for Figures 5b and 7b for the ICRU/AAPM phantom were used for the center and edge measurements, respectively. Their ratio, 76%, lies between the ratios cited for the two standard CTDI phantoms. This is not surprising since the ICRU/AAPM phantom diameter, 30 cm, is also between that for the two standard phantoms. The lower attenuation of polyethylene versus PMMA would also increase the ratio over that for the 32-cm PMMA phantom.

The radial dose distribution is quite different for the infinite scan. When carried out to the limit, the value for $h(L)$ (D_{eq} in Figures 5b and 7b) is actually *higher* at the center than at the edge. Thus the radial dose distribution for the infinite scan, confirmed by Monte Carlo calculations[11], is quite flat and $\overline{D_{eq}}$, the spatially averaged value of D_{eq}, would be around 21 mGy/100 mAs_{eff}. This is a bit over double the 10 mGy/100 mAs_{eff} for the $CTDI_{vol}$ of the 32-cm diameter body phantom. The increase occurs because the long scan allows for a greater relative buildup of scatter along the central axis. In addition, the lower attenuation of the polyethylene and the somewhat smaller diameter of the ICRU/AAPM phantom also make contributions to the increased dose measured along the central axis.

Table 2: All values are from measurements made on the same scanner at 120 kV, the same collimation, and with the same beam-shaping filtration. For the CTDI phantoms, the ratio would be only slightly higher had the 100-mm measurements been made on infinitely long cylinders rather than on cylinders of the standard 15-mm length.[19]

Phantom	*L*	Ratio Description	Ratio Value
32 cm (body) CTDI	100 mm	$CTDI_{100,Ctr}$ / $CTDI_{100,Edge}$	47%
16 cm (head) CTDI	100 mm	$CTDI_{100,Ctr}$ / $CTDI_{100,Edge}$	87%
ICRU/AAPM	100 mm	$h(L)_{Ctr}$ / $h(L)_{Edge}$	76%
ICRU/AAPM	∞	$h(L)_{Ctr}$ / $h(L)_{Edge}$ = $D_{eq,Ctr}$ / $D_{eq,Edge}$	104%

6. Practical Implementation of the Measurement Methodology

This report describes three acquisition configurations. The rationale for this is that using the full phantom provides the full information about D_{eq}; however, this large phantom is cumbersome and impractical for routine use. Therefore, this report describes three tests in which measurements are made:

1. In the full three-section phantom: this may be performed either by the manufacturer in the factory or in a reference lab.
2. In one section of the phantom: this may be performed in the factory/reference lab and verified in the field by a physicist for QC testing.
3. In air (with no phantom): this may also be performed in the factory/reference lab and verified in the field by a physicist for QC testing.

These different testing configurations are summarized in Table 3.

6.1 Measurements in the Full (3 Sections, 60 cm Length) Phantom

Measurement in the full three-section phantom was described in the previous section.

6.2 Measurements in a Single Section of the ICRU/AAPM Phantom

A single section of the phantom is much more practical for performing tests in the field. Because one section is only 200 mm long, the scatter properties of the full 600-mm-long phantom will not be replicated in the shorter phantom. However, measurements in the shorter phantom can be made in the factory and subsequently duplicated in the field by a clinical medical physicist for verification and QC purposes. Comparison (of the integrated dose) to the corresponding factory value validates the use of D_{eq} values and $H(L)$ determined at the factory. Measurements on the single section are to be made using helical scans traversing the complete length of the shorter section [RUN MOVIE # 4]. Both the central and edge values should be established by the manufacturer or reference lab. On acceptance testing, these values should be measured at both positions by the physicist. For annual testing, the central value may suffice, especially if the central value is unique for all bowtie/flat filter combinations.

6.3 Measurements in Air

For consistency or quality control purposes, helical measurements in air [RUN MOVIE # 5] made in the field may be used as a surrogate for in-phantom measurements, subject to specific regulatory and accreditation program requirements.

A setup for air measurements is displayed in Figure 9. The dosimeter is centered in the gantry, and the active volume is positioned beyond the edge of the table (to avoid the effects of table attenuation). Scans are performed by moving the dosimeter completely through the beam, and they are accomplished by moving the table using helical scan settings.

Table 3: Summary of different testing conditions proposed in this report

Test	Phantom	Investigator	Description
1	3 sections (60 cm)	Manufacturer or Reference Lab	Performed in factory or Reference Lab; not for routine QC
2	1 section (20 cm)	Manufacturer or Reference Lab/Physicist	Performed in factory/Ref Lab AND in field; can be done as part of routine QC
3	Air	Manufacturer or Reference Lab/Physicist	Performed in factory/Ref Lab AND in field; can be done as part of routine QC

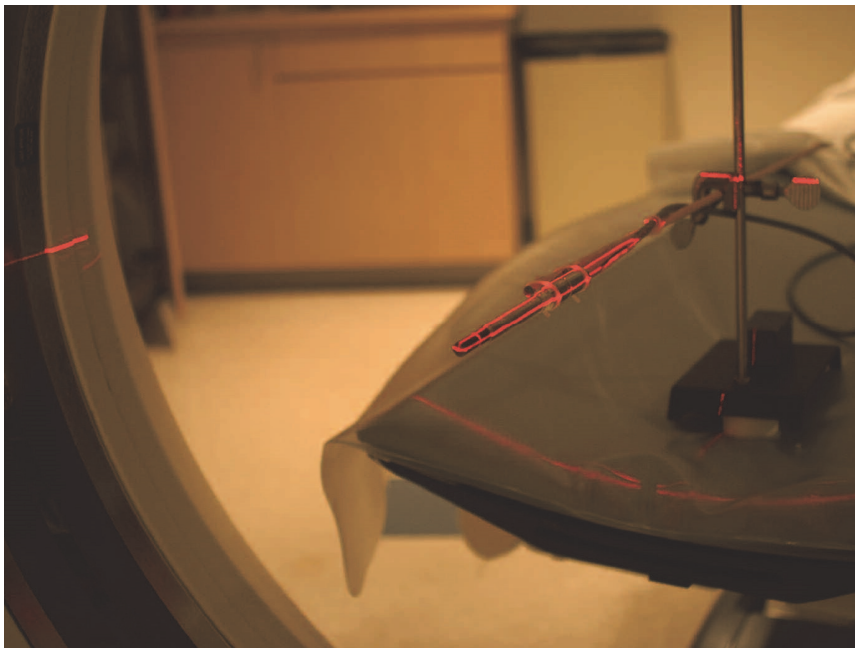


Figure 9. A figure from the TG-111 report. Thimble ionization chamber free-in-air and aligned along the axis of rotation. The chamber is attached to an extender rod from a lab stand, and the assembly is illuminated by the CT system alignment laser lights.

It should be noted that for in-air measurements, one scan per condition (tube potential, bowtie/filter combination—See #4 of Section 4.1) is performed with the dosimeter at isocenter.

In addition to serving as a replacement for actual phantom measurements, in-air measurements can serve other purposes, so it is important that they are made carefully. They can be used to establish tube current linearity—thus allowing a phantom measurement to be made at a tube current and rotation time chosen for convenience—and signal-to-noise considerations. They also can be used to confirm the linear scaling of integrated dose with changes in z-axis collimation aperture a[1], greatly reducing the required number of phantom measurements. (Indeed, this may be the best place to measure or verify the values of a. The vendor's *relative* values of a can be deduced from the $CTDI_{vol}$ or efficiency values displayed on the machine. The air scans present a simple and straightforward method for the verification of the indicated values.)

The integrated value (directly displayed by either the integrating electrometer or the real-time electrometer) is all that is necessary for properly scaling tube current-time product and collimation. A recording of the dose profile in air may be used to verify beam uniformity and with care might be of some value in determining beam width a. However, the finite length of the small chamber needs to be accounted for if used for this purpose. Chamber length is not relevant for determining tube current-time product, effective tube current-time product, or collimation dependence since, as the chamber passes through the beam, every point in the beam is sampled by the entire chamber. Verifying tube current-time product or effective tube current-time product linearity is conveniently done in air (though we recognize that the manufacturers may have established more direct and precise means for doing this).

It is understood that the in-air measurements, as described, sample the beam only along the axis of rotation. In principle, it is possible that two bowtie designs would have the same central beam properties and yet be quite different when the entire beam is explored. We do not expect this coincidental

behavior to be of much consequence for annual physics testing. However, in order to eliminate this possibility in acceptance testing, the single-section test described for acceptance testing in section 5.2 should be performed along with the air measurement. As in section 5.2, if the air measurement is unique for each bowtie/flat filter combination, the air measurement should suffice for annual physics testing. If there *is* an ambiguity, an off-axis air measurement[12] could be used to resolve any equivocality.

6.4 Measurements in Very Wide Beams and Using Stationary Tables

An example CT system with a very wide (e.g., 16 cm) beam width is the Toshiba Aquilion ONE. In the helical scan mode this machine may be tested as described in the procedure above for beam widths up to 8 cm. The full detector width of 16 cm is used only with a stationary table in the volume acquisition mode. Although Dixon and Boone[5] have rigorously demonstrated self-consistency between the two types of scans, an alternative—the pseudohelical scan method described by Lin and Herrnsdorf[13]—has been specifically developed for acquiring dK/dz using a stationary table with the tube on and with the gantry continuously rotating continuously rotating [RUN MOVIE # 6]. This is a special case of the single scan method. Here the dosimeter is mounted on an assembly that is pushed or pulled at constant speed through the phantom. In this case, the dosimeter channels must pass completely through the phantom, end to end. One way to accomplish this is to assemble the phantom from three sections of type A. For the edge position at 12 o'clock, high spatial frequency modulation is best achieved by moving the dosimeter slowly through the phantom along with the utilization of a high gantry rotation frequency. (This may be thought of as using a low pseudopitch.) This results in high-frequency sampling of the dose profile envelope. The limiting dose D_{eq} and approach to equilibrium function $H(L)$ are determined in precisely the same way as they are for the helical scans described above.

There is also a form of the serial method that can be implemented for this special case. This is described in AAPM Report 111 where the notion of irradiated length is utilized when a scan is made with a stationary table and a wide beam. Here the dosimeter is positioned in the central plane of the phantom, as before, and the phantom is centered in the beam. The integrated dose per rotation is determined. The length L is simply the width of the beam. The point $h(L)$ is thus determined for each value of L used. L may be defined, for example, as the FWHM of the beam along the central axis, or it may be deduced by comparison of measurements using a long helical scan. Without moving the phantom, this limits us to values of L up to that of the widest beam available, a_w. This limitation presents problems in establishing D_{eq}. One way to obtain $h(L)$ for values of L that go beyond a_w and capture more of the scatter tail is to do the following:

1. First be sure that $h(a_w)$ has been determined.
2. Choose a beam width a^* for the scanner (where $a^* \leq a_w$).
3. Translate the phantom (in the z direction) so that the dosimeter is positioned at $z = a_w/2 + a^*$. (The dosimeter remains in the central plane of the phantom; the phantom is no longer centered in the beam.)
4. Perform a fixed-table scan (with the same techniques used to acquire $h(L)$ for values of $L < a_w$) and record the reading on the dosimeter.
5. Move the phantom and dosimeter to the opposite side of the scanning plane, i.e., to $z = -(a_w/2 + a^*)$.
6. Repeat step 3.

7. Add the two readings from steps 3 and 5 to the value recorded for $L = a_w$. This will be $h(a_w + 2a^*)$.

When establishing position, it will be important to match the half-maximum end points of a_w and a^*. This method can be used to extend L up to $3a_w$ and then extended again to go from $L = 3a_w$ to $L = 5a_w$, $7a_w$, etc. Clearly, if possible to implement, a single-scan method is much preferred.

7. Conclusions

By extending the scan length to that required for approaching the limiting value, D_{eq}, the ICRU/AAPM phantom and measurement techniques described here address, in a simple and natural way, the limitations of the CTDI methodology presented in the introduction. These include the systematic exclusion of dose accumulating for scans longer than 100 mm, exclusion of primary beam for scanners with beam widths in excess of 100 mm, and potential unsuitability for stationary table applications. Together, D_{eq} and the remarkably robust "approach to equilibrium function" $H(L)$ promise to present a simple and intuitive picture describing the radiation output of the machine by describing it in terms of the dose to a standard (infinite) phantom. Further, a high correlation between D_{eq} and CTDI measurements has been demonstrated[4,14]. This is not altogether surprising, since both are indicators of machine output. This correlation will facilitate the adoption of the ICRU/AAPM phantom as a future standard.

8. References

1 American Association of Physicists in Medicine. "Comprehensive methodology for the evaluation of radiation dose in x-ray computed tomography." Report of AAPM Task Group 111: The Future of CT Dosimetry. College Park, MD: AAPM, 2010.

2 Boone, J. M. (2007). "The trouble with CTDI100." *Med. Phys.* 34(4):1364–71.

3 Attix, F. H. *Introduction to Radiological Physics and Radiation Dosimetry*. New York: John Wiley & Sons, Inc., 1986.

4 Boone, J. M., et al. (2012). "CT Dosimetry in Phantoms." In ICRU Report 87, Radiation Dose and Image-Quality Assessment in Computed Tomography. *JICRU* 12(1):67–87.

5 Dixon, R. L. and J. M. Boone. (2010). "Cone beam CT dosimetry: A unified and self-consistent approach including all scan modalities—With or without phantom motion." *Med. Phys.* 37(6):2703–18.

6 International Electrotechnical Commission. Glossary. Available at std.iec.ch/glossary. Search for "doselength product" and select "English."

7 Data and analysis by Sarah McKenney.

8 DICOM Standard of NEMA PS3 / ISO 12052. Part 16. Digital Imaging and Communications in Medicine (DICOM) Standard. Rosslyn, VA: National Electrical Manufacturers Association. Available free at https://www.dicomstandard.org/.

9 Dixon, R. L. (2003). "A new look at CT dose measurement: Beyond CTDI." Med. Phys. 30(6):1272–80.

10 Dixon, R. L., M. T. Munley, and E. Bayram. (2005). "An improved analytical model for CT dose simulation with a new look at the theory of CT dose." *Med. Phys.* 32(12):3712–28.

11 Bakalyar, D. M., W. Feng, and S. McKenney. (2014). "Diameter Dependency of the Radial Dose Distribution in a Long Polyethylene Cylinder." *Med. Phys.* 41:405.

12 Boone, J. M. (2009). "Method for evaluating bow tie filter angle-dependent attenuation in CT: Theory and simulation results." *Med. Phys.* 37(3):40–48.

13 Lin, P. J. and L. Herrnsdorf. (2010). "Pseudohelical Scan for the Dose Profile Measurements of 160-mm-Wide Cone-Beam MDCT." *AJR*194:897–902.
14 McKenney, SE. "Computed Tomography Dose and Image Quality Characterization Using Real-Time Dosimeter Measurements." (Doctoral dissertation). Retrieved from ProQuest Dissertations Publishing (Accession No. 3614244); 2013.
15 American Association of Physicists in Medicine. "Use of Water Equivalent Diameter for Calculating Patient Size and Size-Specific Dose Estimates (SSDE) in CT." Report of AAPM Task Group 220: Determination of a Patient Size Metric for CT Size Specific Dose Estimation. College Park, MD: AAPM, 2014.
16 American Association of Physicists in Medicine. "Size Specific Dose Estimates (SSDE) in Pediatric and Adult CT Examinations." Report of AAPM Task Group 204. College Park, MD: AAPM, 2011.
17 Ford, E. S., L. M. Maynard, and C. Li. (2014). "Trends in Mean Waist Circumference and Abdominal Obesity Among US Adults, 1999–2012." *JAMA* 312(11):1151–53.
18 Bakalyar, D. M. (2016). "In Search of Infinity: Finding the Limiting Dose for An Infinite CT Scan On a Cylinder of Finite Length." *Med. Phys.* 43(6):3395.
19 Dixon, R. L. and A. C. Ballard. (2007). "Experimental validation of a versatile system of CT dosimetry using a conventional ion chamber: Beyond CTDI100." *Med. Phys*. 34(8):3399–413.

Appendix I:

Measurements in Other Geometries

Even though related systems (e.g., C-arm cone-beam CT) have much in common with MDCT, special challenges place the application of our methodology to these systems well beyond the scope of this report. These problems include, but are not limited to, sub-360° acquisition and the inability for the operator to directly control the tube potential. Also, in many cases, the extent of the beam in the *xy* plane is such that it does not intercept the entire patient. For example, it is often only 25 cm, whereas in diagnostic CT machines, the beam can usually span 50 cm for body scans. So, for the ICRU/AAPM phantom as well as the 32-cm CTDI body phantom an outer circular region of the phantom is not irradiated in the same way as the inner part [RUN MOVIE # 7]. This is acceptable for imaging if only the inner part is of interest. However, the radial behavior of the dose profile will differ from that of a phantom completely enveloped by a broad beam, and further study may be necessary to properly estimate $\overline{D}_{eq}$ in these systems. (A smaller-diameter phantom is a partial solution but leaves unaddressed the problem of dose delivery when the breadth of a body is not contained within a beam—an occasional problem in MDCT but common in these other systems.)

Appendix 2:

Measurement Equipment Note

The serial method has been successfully applied using small ion chambers (Model 2571 Farmer chamber) by several members of TG-200. Small solid-state dosimeters with their potentially high spatial resolution and sensitivity, coupled with appropriate recording electronics, present another possibility for the single-scan method. It should be noted that such devices may present some unique challenges. The first is that the device may be sensitive to energy dependencies (e.g., beam hardening). For measurements performed at the edge position, the change in energy spectrum caused by the phantom can vary significantly during gantry rotation. Therefore, if this device is to be used in the single-scan method, care should be taken and the manufacturer consulted to ensure the proper corrections are used.

Ironically, the high spatial resolution that can be a desirable feature of these small dosimeters may mean that the pitch criterion noted at the end of section 4.3 is not met. One possible solution for this problem is to average several scans together with the dosimeter position shifted slightly (in the z direction) relative to the phantom for each scan. Here it is necessary to take care that the *dosimeter* positions (or, equivalently, dK/dz envelope positions) are matched for the different scans prior to averaging.

Appendix 3:

Supplemental Material Available

Data Recording

A sample Excel workbook, ICRU-AAPM_phantom.xlsx, is provided. This may be modified as experience, need, or convenience dictates. Note that for each kV, only one set of data measurements using the phantom is required. Additional rows in the spreadsheet are for air measurements at different collimation settings or at settings designed to check the linearity of tube current, rotation time, or effective tube current-time product. Separate blank sheets are provided for determining $H(L)$ for each tube potential. A sample dose profile and integral is included with notes.

Animations

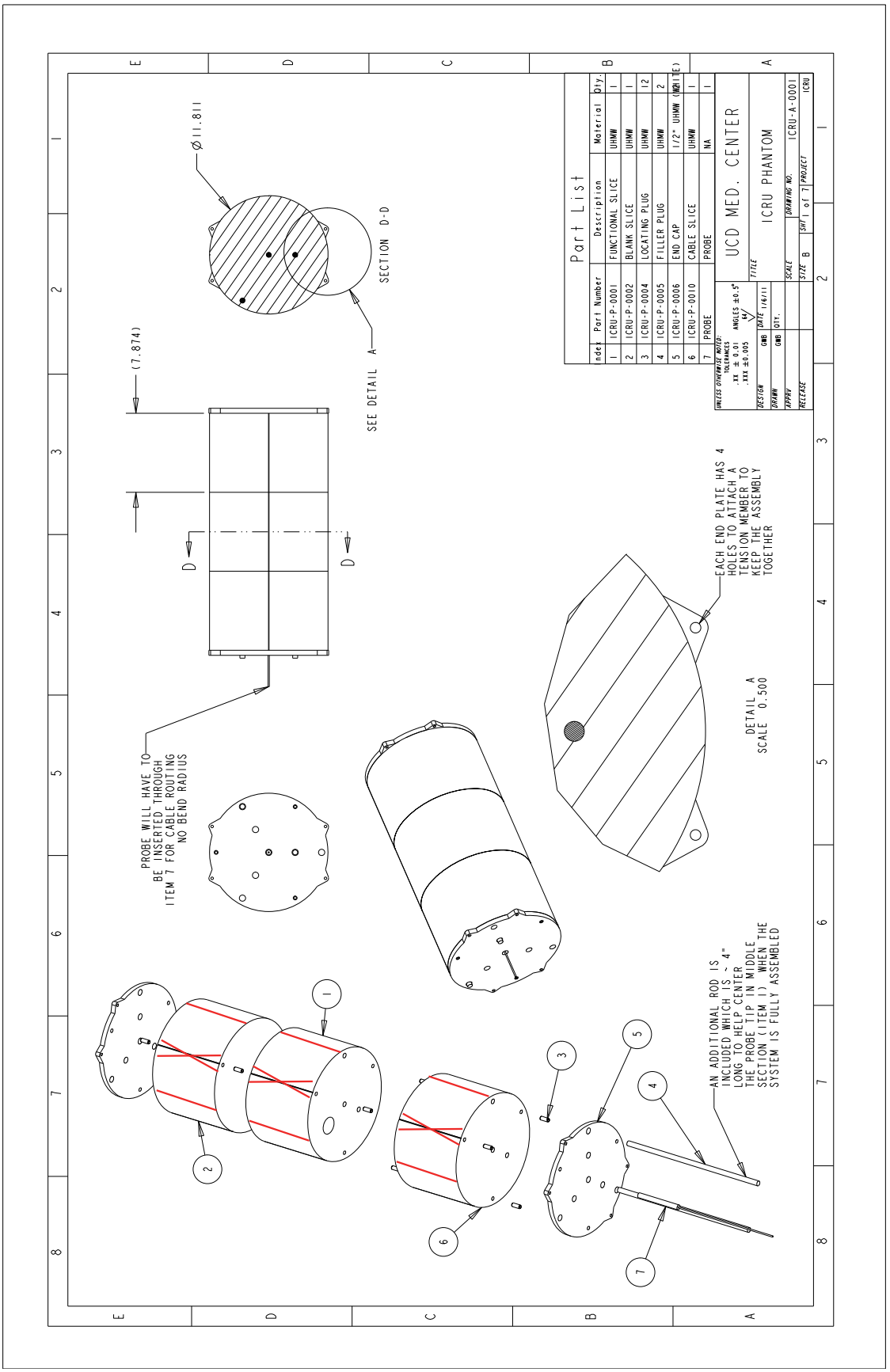
References to seven animations are found in this report. Look for the words [RUN MOVIE] in brackets. By clicking on this text, a hyperlink will take you to the AAPM website where the animations are stored and can be played.

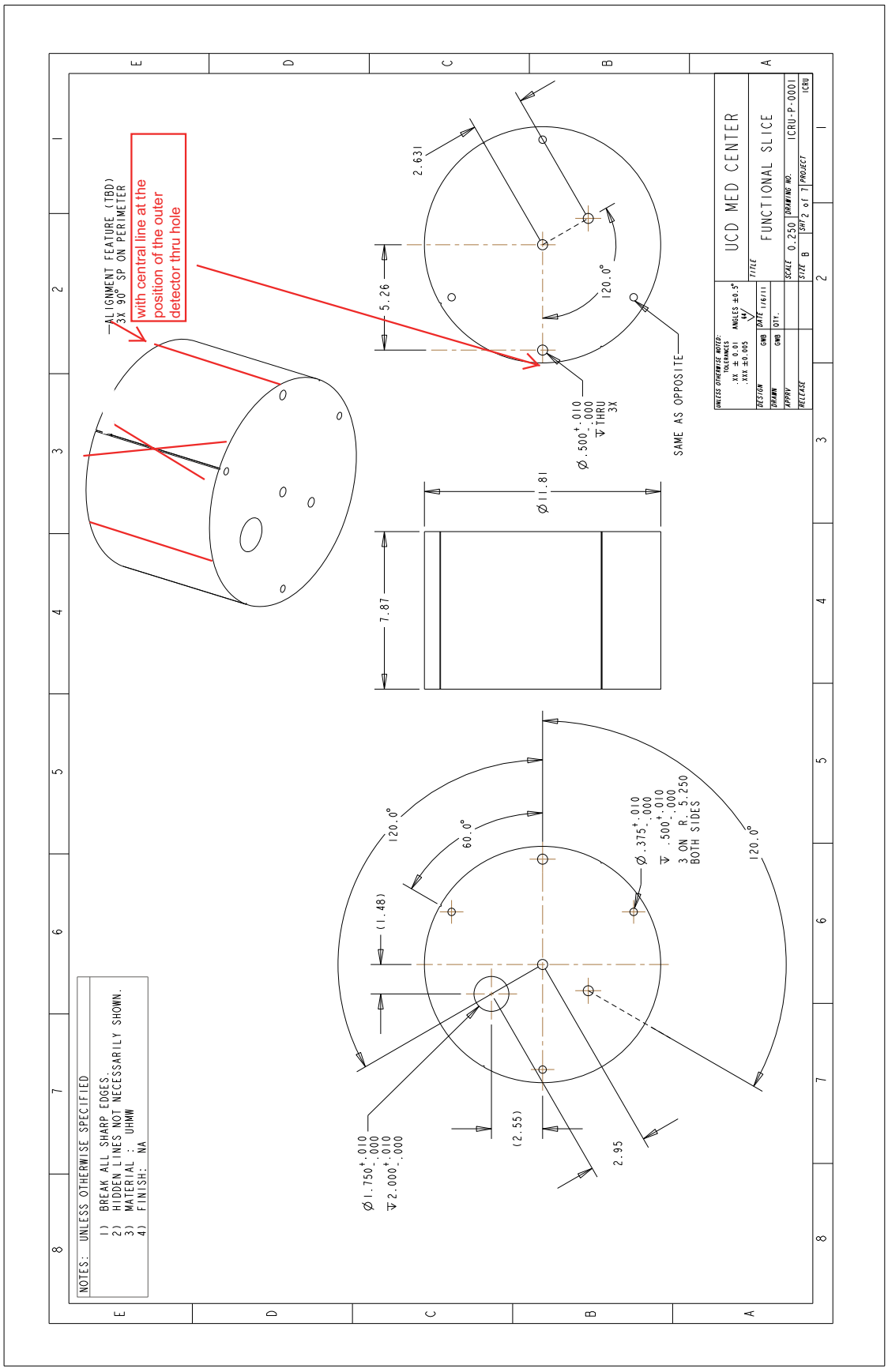
Tutorial and Example for Fine-Tuning the Determination of D_{eq}.

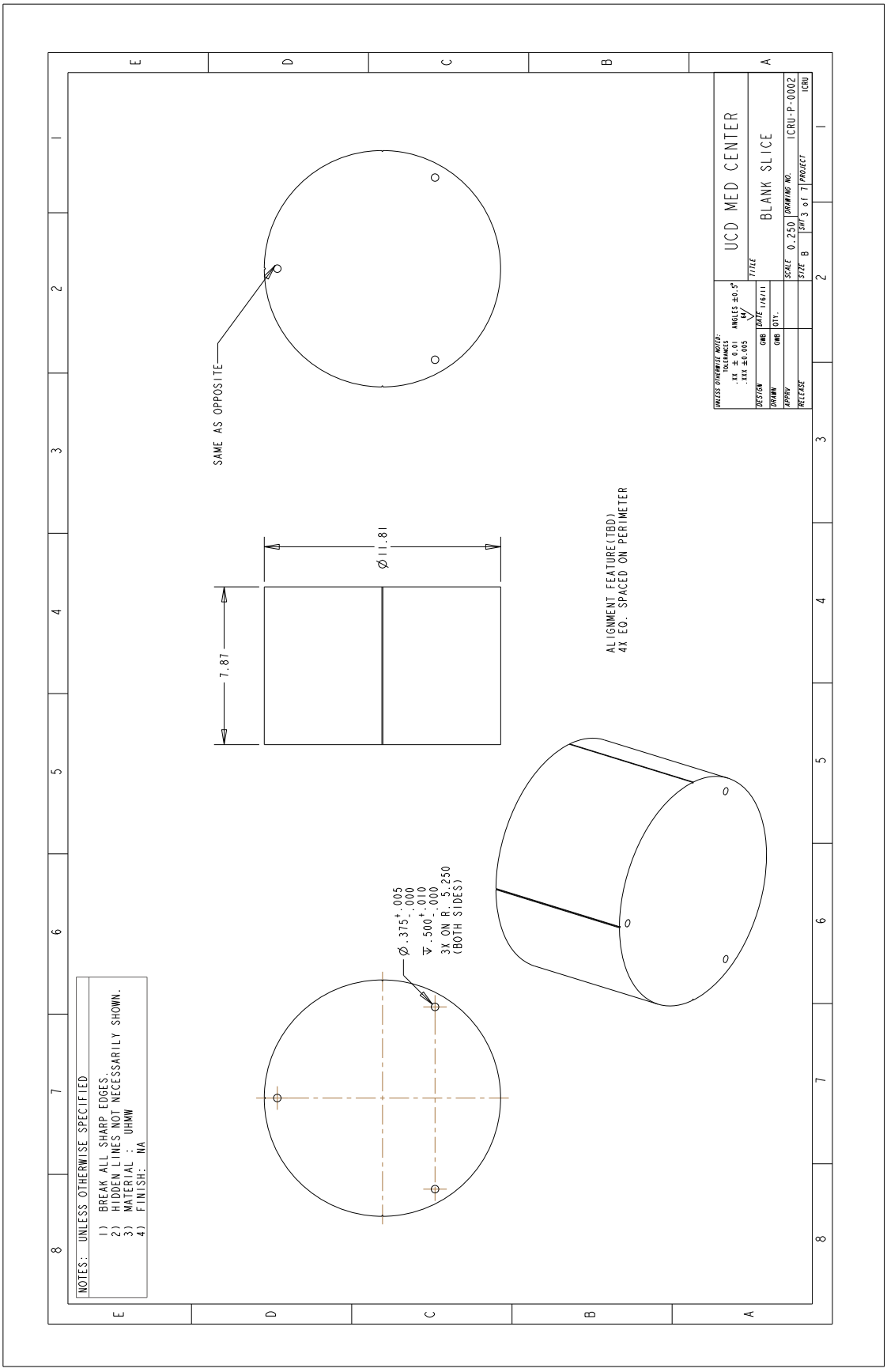
An Excel workbook and a brief document are included for augmenting the discussion in Appendix 5.

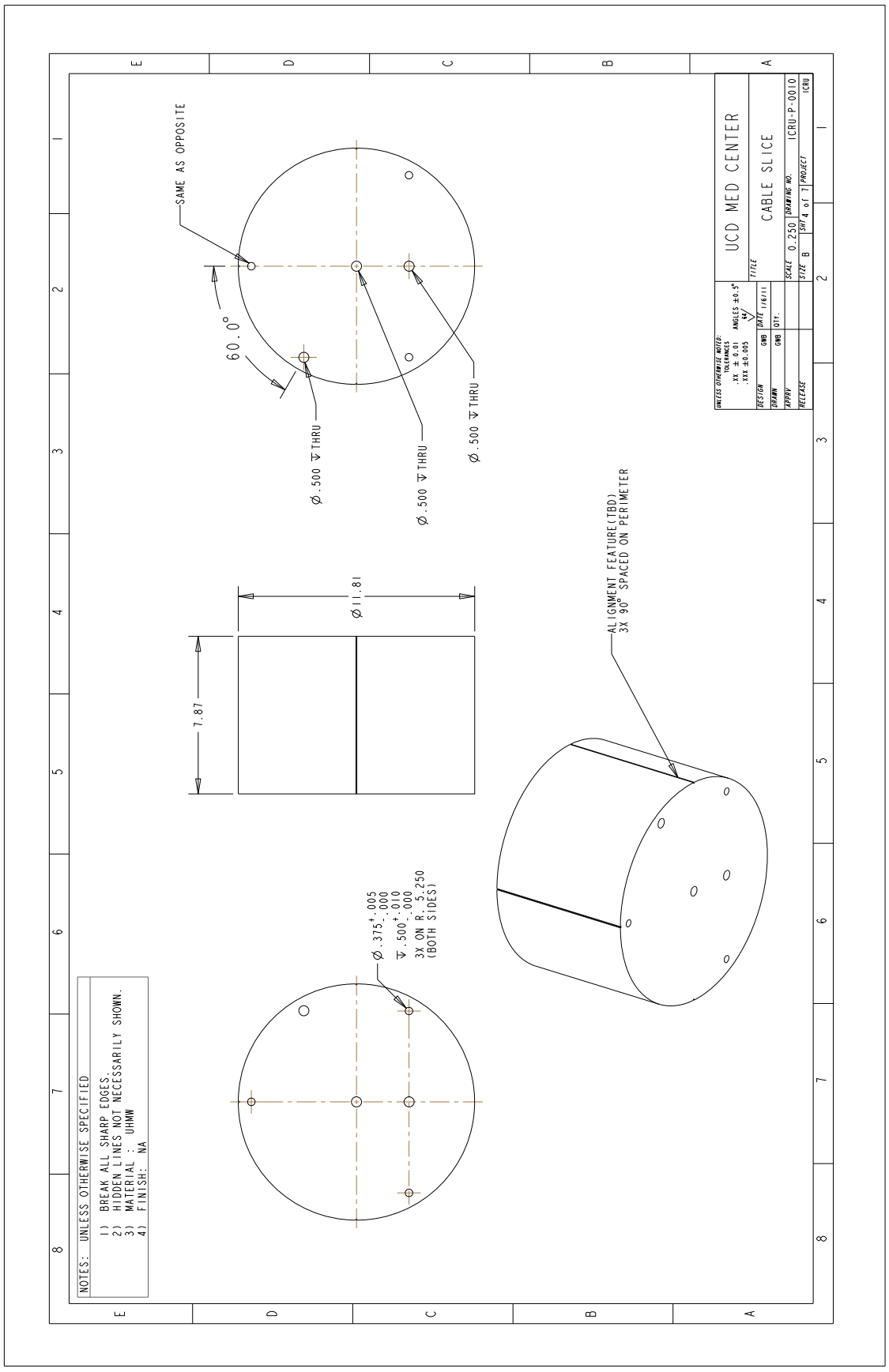
Machine Drawings for Phantom

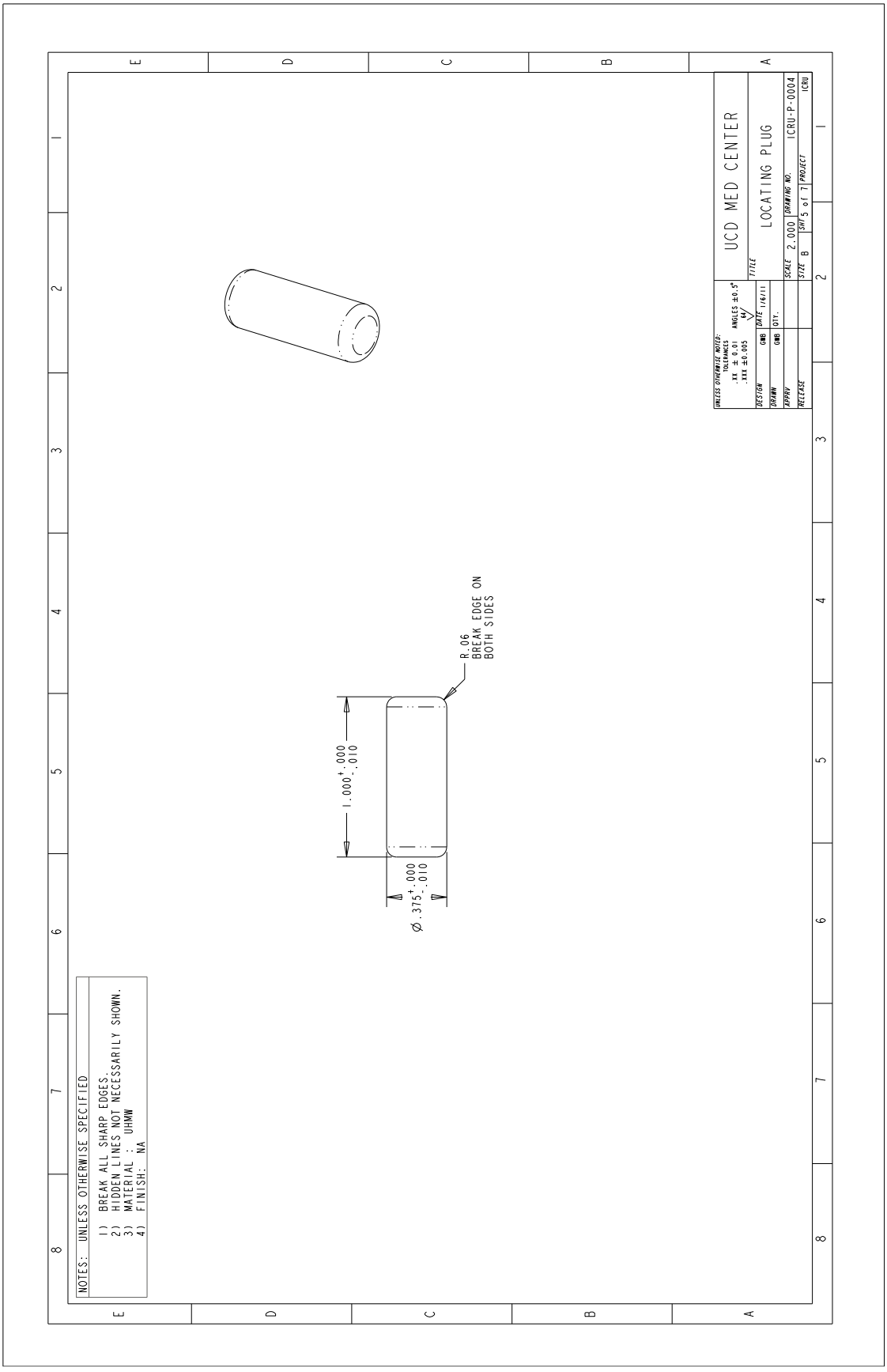
See the next four pages for phantom construction drawings.

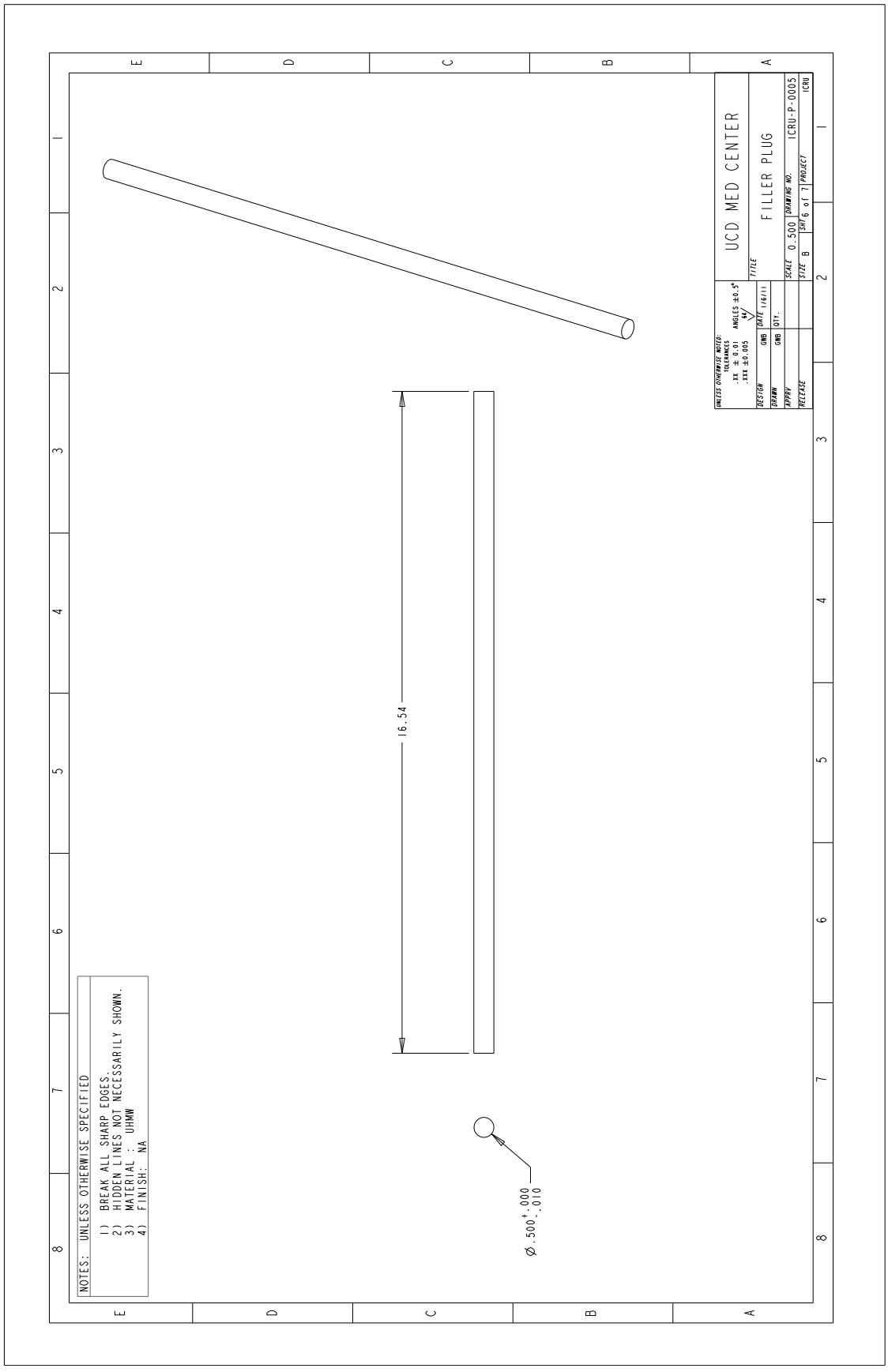

Part List
Index | Part Number | Description | Material | Qty.
1 | ICRU-P-0001 | FUNCTIONAL SLICE | UHMW | 1
2 | ICRU-P-0002 | BLANK SLICE | UHMW | 1
3 | ICRU-P-0004 | LOCATING PLUG | UHMW | 12
4 | ICRU-P-0005 | FILLER PLUG | UHMW | 2
5 | ICRU-P-0006 | END CAP | 1/2" UHMW (WHITE) | 1
6 | ICRU-P-0010 | CABLE SLICE | UHMW | 1
7 | PROBE | PROBE | NA | 1
UNLESS OTHERWISE NOTED: TOLERANCES .XX ± 0.01 .XXX ±0.005 ANGLES ±0.5°
DESIGN GMB DATE 1/6/11
DRAWN GMB QTY.
APPROV
RELEASE
UCD MED. CENTER
TITLE ICRU PHANTOM
SCALE
SIZE B
DRAWING NO. ICRU-A-0001
SHT 1 of 7 PROJECT ICRU
Ø11.811
SECTION D-D
SEE DETAIL A
(7.874)
D
D
PROBE WILL HAVE TO BE INSERTED THROUGH ITEM 7 FOR CABLE ROUTING NO BEND RADIUS
EACH END PLATE HAS 4 HOLES TO ATTACH A TENSION MEMBER TO KEEP THE ASSEMBLY TOGETHER
DETAIL A
SCALE 0.500
AN ADDITIONAL ROD IS INCLUDED WHICH IS ~4" LONG TO HELP CENTER THE PROBE TIP IN MIDDLE SECTION (ITEM 1) WHEN THE SYSTEM IS FULLY ASSEMBLED
1
2
3
4
5
6
7

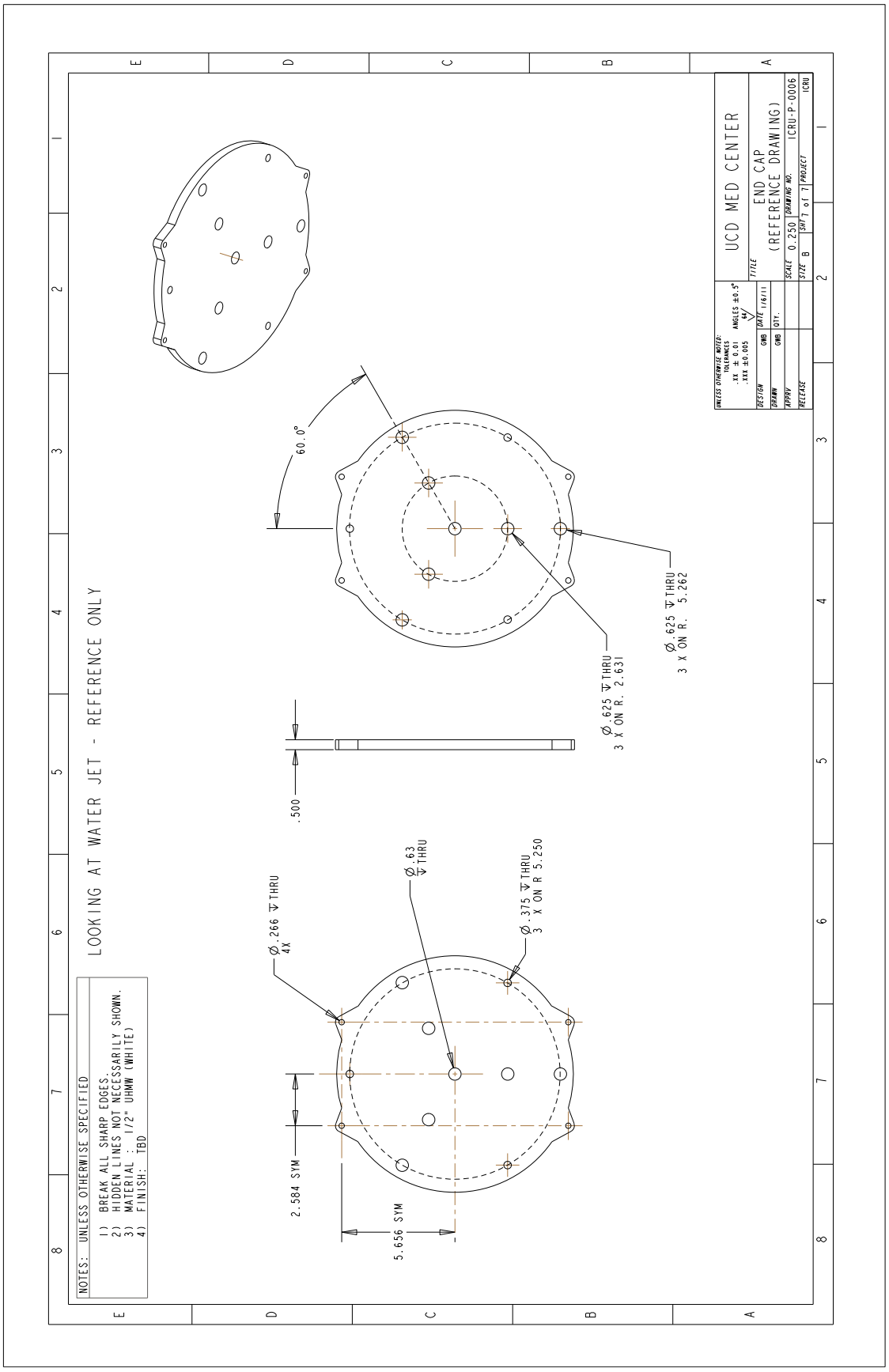

with central line at the position of the outer detector thru hole
ALIGNMENT FEATURE (TBD)
3X 90° SP ON PERIMETER
2.631
5.26
120.0°
Ø.500 +.010 -.000 ∓ THRU 3X
SAME AS OPPOSITE
Ø11.81
7.87
120.0°
60.0°
(1.48)
Ø.375 +.010 -.000
∓ .500 +.010 -.000
3 ON R 5.250
BOTH SIDES
120.0°
Ø1.750 +.010 -.000
∓2.000 +.010 -.000
(2.55)
2.95
NOTES: UNLESS OTHERWISE SPECIFIED
1) BREAK ALL SHARP EDGES.
2) HIDDEN LINES NOT NECESSARILY SHOWN.
3) MATERIAL : UHMW
4) FINISH: NA
UCD MED CENTER
FUNCTIONAL SLICE
SCALE 0.250
DRAWING NO. ICRU-P-0001
SIZE B
SHT 2 of 3
PROJECT ICRU


UCD MED CENTER
BLANK SLICE
ICRU-P-0002
SCALE 0.250
SIZE B
SHT 3 of 7
PROJECT
ICRU
UNLESS OTHERWISE NOTED:
DIMENSIONS ARE IN INCHES
.XX ± 0.01
.XXX ±0.005
ANGLES ±0.5°
DESIGN GMB
DRAWN GMB
APPRV
RELEASE
QTY.
DATE 1/6/11
SAME AS OPPOSITE
Ø11.81
7.87
ALIGNMENT FEATURE(TBD)
4X EQ. SPACED ON PERIMETER
Ø.375 +.005 -.000
⌖.500 +.010 -.000
3X ON R.5.250
(BOTH SIDES)
NOTES: UNLESS OTHERWISE SPECIFIED
1) BREAK ALL SHARP EDGES.
2) HIDDEN LINES NOT NECESSARILY SHOWN.
3) MATERIAL : UHMW
4) FINISH: NA


SAME AS OPPOSITE
60.0°
Ø.500 ↧THRU
Ø.500 ↧THRU
Ø.500 ↧THRU
Ø11.81
7.87
ALIGNMENT FEATURE(TBD)
3X 90° SPACED ON PERIMETER
Ø.375 +.005 -.000
↧.500 +.010 -.000
3X ON R5.250
(BOTH SIDES)
NOTES: UNLESS OTHERWISE SPECIFIED
1) BREAK ALL SHARP EDGES.
2) HIDDEN LINES NOT NECESSARILY SHOWN.
3) MATERIAL : UHMW
4) FINISH: NA
UCD MED CENTER
CABLE SLICE
ICRU-P-0010


UCD MED CENTER
LOCATING PLUG
ICRU-P-0004
NOTES: UNLESS OTHERWISE SPECIFIED
1) BREAK ALL SHARP EDGES.
2) HIDDEN LINES NOT NECESSARILY SHOWN.
3) MATERIAL : UHMW
4) FINISH: NA
R.06 BREAK EDGE ON BOTH SIDES
1.000 +.000 -.010
Ø.375 +.000 -.010


UCD MED CENTER
FILLER PLUG
ICRU-P-0005
16.54
Ø.500 +.000 -.010
NOTES: UNLESS OTHERWISE SPECIFIED
1) BREAK ALL SHARP EDGES.
2) HIDDEN LINES NOT NECESSARILY SHOWN.
3) MATERIAL : UHMW
4) FINISH: NA


UCD MED CENTER
END CAP
(REFERENCE DRAWING)
ICRU-P-0006
SCALE 0.250
SIZE B
SHT 1 of 1
PROJECT
ICRU
UNLESS OTHERWISE NOTED:
.XX ± 0.01
.XXX ±0.005
ANGLES ±0.5°
DESIGN GMB 1/6/11
DRAWN GMB
APPRV
RELEASE
NOTES: UNLESS OTHERWISE SPECIFIED
1) BREAK ALL SHARP EDGES.
2) HIDDEN LINES NOT NECESSARILY SHOWN.
3) MATERIAL : 1/2" UHMW (WHITE)
4) FINISH: TBD
LOOKING AT WATER JET - REFERENCE ONLY
60.0°
Ø.625 ↧ THRU
3 X ON R. 2.631
Ø.625 ↧ THRU
3 X ON R. 5.262
.500
Ø.266 ↧ THRU
4X
Ø.63
↧ THRU
Ø.375 ↧ THRU
3 X ON R 5.250
2.584 SYM
5.656 SYM

Appendix 4:

Corresponding Human Size using Water-Equivalent Diameter

It is instructive to look at the water-equivalent diameter d_w discussed at length in AAPM Report No. 220[15]. This is the diameter of a water cylinder having the same mean absorbed dose as the section of the patient or phantom under consideration. AAPM Report No. 220 expands the concept of size-specific dose estimate (SSDE) described in AAPM Report No. 204[16] to include, in addition to geometry, the effects of the composition and density of the imaged tissue. Utilizing Equation 4 from AAPM Report No. 220,

$$d_w = 2\sqrt{\frac{A_w}{\pi}} = 2\sqrt{\frac{A_\kappa}{\pi}\left(1+\frac{\kappa}{1000}\right)} = d_\kappa\sqrt{\left(1+\frac{\kappa}{1000}\right)}, \tag{4}$$

where κ is the area-average CT number for the cross-sectional area A_κ of the subject (patient or phantom) under consideration. (The definition of d_κ in terms of A_κ is implicit in Equation 4.) With water equivalence as a metric, we equate the water-equivalent diameter of our phantom to the diameter corresponding to the waist of human subjects. Thus,

$$d_H\sqrt{\left(1+\frac{\kappa_H}{1000}\right)} = d_P\sqrt{\left(1+\frac{\kappa_P}{1000}\right)}, \tag{5}$$

where d_H and d_P are the human and phantom diameters and κ_H and κ_P are the corresponding CT numbers. For all phantoms under consideration and in the region of the waist, $|\kappa|$ is $\ll 1000$, which allows us to expand the radicals in Equation 5 to lowest order in $\kappa/1000$. Rearranging terms,

$$d_H = d_P\left(1+\frac{\kappa_P-\kappa_H}{2000}\right). \tag{6}$$

How do our phantoms correspond to waist size? A recent study[17] puts the current average (men and women combined) waist size at 98.5 cm (38.7 inches) with the measurements being made just above the iliac crest. (Note that the point of this publication is that the average waist size has increased significantly over the last decade and that 98.5 cm is an *average*, not an ideal.) The area average CT number (κ_H in Equations 5 and 6) is around zero at the waist. For the 30-cm-diameter ICRU/AAPM phantom, κ_P was –74 for the scans used for Figures 5 and 7. Substituting into Equation 6, this corresponds to a human waist size of

$$C_{H,TG200} = \pi\times 30\text{ cm}\times\left(1+\frac{-74-0}{2000}\right) = 94.2\text{ cm}\times 0.96 = 90.8\text{ cm} \tag{7}$$

(36 inches). The 32-cm CTDI phantom corresponds to a larger person, more likely one with significant body fat. Set κ_H to –40 to account for the additional adipose tissue in many of these larger people. The CT number for PMMA is around 124. Again substituting into Equation 6, the 32-cm CTDI phantom corresponds to a human waist size of

$$C_{H,CTDI} = \pi\times 32\text{ cm}\times\left(1+\frac{124-(-40)}{2000}\right) = 101\text{ cm}\times 1.08 = 109\text{ cm} \tag{8}$$

(43 inches). Using this metric, the ICRU/AAPM phantom represents a moderate waist size for western populations, whereas the CTDI phantom better characterizes individuals somewhat larger than average. Both are well within the normal range of adult waist sizes in western populations.

Appendix 5:

Fine Tuning D_{eq}

Figures 4, 5b, 6, and 7b show that $h(L)$ is closing in on its limiting value D_{eq} when the entire 600 mm of the phantom is scanned. However, it is clear that even at this length (see Section 4.1) $h(L)$ is still increasing, i.e., a slightly higher dose would result from a scan through a longer phantom. In what follows, we describe a method for including this residual dose, giving us a more accurate assessment of D_{eq}.

In its simplest form, the $h(L)$ curve is known to be that of an exponential rise (like that of a charging capacitor) to a limiting value which, in our case, is D_{eq}. That is,

$$h(L) = D_{eq}\left[1-\alpha\ \exp(-4L / L_{eq})\right] = D_{eq}\left[1-\alpha 2^{-L/L_{½}}\right] \tag{9}$$

where $L_{½}$ is the value of L for which the exponential in Equation 9 is equal to ½. $D_{eq}(1–\alpha)$ is the value for h when $L = 0$.

$$L_{eq} = \frac{4}{\ln(2)} L_{½} = 5.77\, L_{½} \tag{10}$$

is the finite scanning length for which AAPM Report 111 suggests that the cumulative dose is close enough to D_{eq} for practical purposes. The two forms of Equation 9 are equivalent, but the second form is more convenient for what follows. Rearranging,

$$\left[1-\frac{h(L)}{D_{eq}}\right] = \alpha\ 2^{-L/L_{½}}\ . \tag{11}$$

Next define the function $g(L, D^*)$ using the following relationship:

$$g(L, D^*) \equiv \log_2\left[1-\frac{h(L)}{D^*}\right]. \tag{12}$$

Take the logarithm (base 2) of Equation 11. Then, using the definition in Equation 12,

$$g(L, D_{eq}) = \log_2 \alpha - \frac{L}{L_{½}}\ , \tag{13}$$

which is a straight line (with L as the abscissa and g as the ordinate) as long as $h(L)$ follows the form of an exponential rise to a limit. Because base 2 was used in taking the logarithm, each increase in L by the half-length $L_{½}$ results in a decrease in g by 1. (This decrease by 1 corresponds to a reduction of the distance between $h(L)$ and its asymptotic limit D_{eq} by half.)

On the other hand, if D^* does *not* equal D_{eq}, a plot of $g(L, D^*)$ versus L will deviate from a straight line. This gives us a means of determining the best estimate of D_{eq} from $h(L)$. As an example, consider Figure 10, which uses the experimentally determined $h(L)$ from Figure 5. First assume that following a scan of the entire phantom, the dose has essentially reached its limiting value and set $D^* = h(600\text{ mm}) = 21.87$ mGy/100 mAs_{eff}. The plot of g for this value of D^* is the blue line in Figure 10; the curvature is obvious, and the coefficient of determination (R^2)—which we can get by using the Trendline option in Excel—is only 0.92. By trial and error, we can get the very straight line shown in

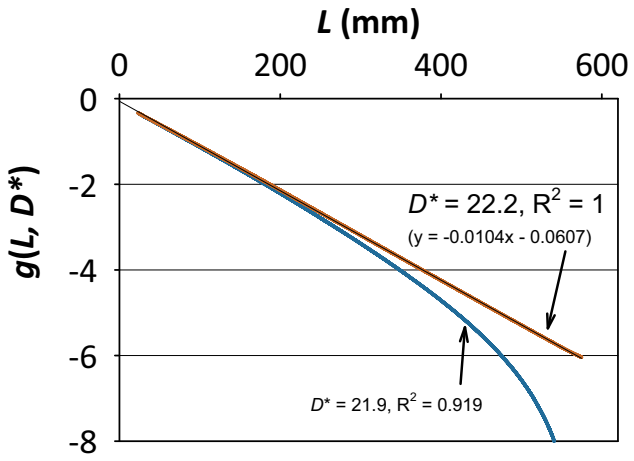


Figure 10. A plot of L versus $g(L,D^*)$. D^* was adjusted to give the best fit to a straight line. This occurs when a value of 22.21 mGy/100 mAs_{eff} is chosen. The curve for D^* set to h(600 mm) = 21.9 mGy/100 mAs_{eff} is shown for comparison. The regression line and linear parameters are displayed using Excel's Trendline tools.

red. Here D is set equal to 22.21 mGy/100 mAs_{eff}, which we now take to be our best estimate of D_{eq}. From Equation 13 and the linear fit parameters displayed on the graph, $\log_2\alpha = -0.607$ and $1/L_{½} = 0.0104$. (The linear fit parameters and R^2 values are obtained using Excel's Trendline tools.) With these along with the best value of D_{eq}, Equation 9 becomes

$$h(L) = 22.21 \text{ mGy}\left[1 - 0.959 \times 2^{(-L/96.15 \text{ mm})}\right] \text{ per } 100 \text{ mAs}_{\text{eff}} \ . \tag{14}$$

With practice, trial-and-error works quite well, but curve fitting with Excel's Solver is easy to implement and delivers the best estimate for D_{eq} quickly and automatically using iteration. A separate Excel spreadsheet and brief document illustrating this method are included as supplemental material.

This analysis was repeated for several more scans with the results listed in Table 4. The corresponding figure for each row of data is given in the first column: Figure 5 for the data just described, Figure 7 for the edge data, and Figure 4 for the data acquired on a Siemens AS+ scanner. For completeness, the data acquired by scanning through the intermediate channel of the phantom is also shown (but with no corresponding figure). This intermediate channel is at a radius of 6.68 cm.

Table 4: The result of fine tuning D_{eq} for the scans described in Figures 5, 7, and 4. For completeness, the results from the scan through the intermediate channel, at a radius halfway (6.68 cm) between those of the center and edge channels, of the ICRU/AAPM phantom are also displayed. The units are displayed between parentheses of the header row where appropriate. Three of the scans were on a Philips Brilliance 6; the other scan was on a Siemens AS+.

Figure	Description	h(600 mm) (mGy/100 mAs$_{eff}$)	D_{eq} (mGy/100 mAs$_{eff}$)	$1/L_{½}$ (mm^{-1})	$\log_2(\alpha)$	$L_{½}$ (mm)	α	$h(600)/D_{eq}$
5	Center (Philips)	21.89	22.21	0.0104	–0.0607	96.15	0.959	98.5%
7	Edge (Philips)	20.98	21.16	0.0105	–0.9550	95.24	0.516	99.2%
–	Intermediate (Philips)	22.18	22.47	0.0105	–0.1729	95.50	0.887	98.7%
4	Center (Siemens)	14.70	14.89	0.0103	–0.1130	96.90	0.925	98.7%

Note that the half-length $L_{½}$ is virtually the same for all the scans listed. (This is consistent with the L dependence for an analytic fit to Monte Carlo data.) The earlier approach to D_{eq} in Figure 7 versus Figure 5 is due to the lower value for α. From Equation 9, this means that for the edge scan, $h(L)$ has a "head start" toward equilibrium; it's already closer to D_{eq} at $L = 0$.